bioRxiv preprint doi: https://doi.org/10.1101/2020.09.04.283739; this version posted September 4, 2020. The copyright holder for this preprint (which was not certified by peer review) is the author/funder. All rights reserved. No reuse allowed without permission.

Resolving the spatial and cellular architecture of lung adenocarcinoma by multi-region single-cell sequencing

Ansam Sinjab [1]*, Guangchun Han [2]*, Kieko Hara [1], Warapen Treekitkarnmongkol [1], Patrick Brennan [3], Minghao Dang [2], Dapeng Hao [2], Ruiping Wang [2], Enyu Dai [2], Hitoshi Dejima [1], Jiexin Zhang [4], Elena Bogatenkova [3], Beatriz Sanchez-Espiridion [1], Kyle Chang [5], Danielle R. Little [6], Samer Bazzi [7], Linh Tran [8], Kostyantyn Krysan [8], Carmen Behrens [9], Dzifa Duose [1], Edwin R. Parra [1], Maria Gabriela Raso [1], Luisa M. Solis [1], Junya Fukuoka [10], Jianjun Zhang [9], Boris Sepesi [10], Tina Cascone [9], Lauren Byers [9], Don L. Gibbons [9], Jichao Chen [6], Seyed Javad Moghaddam [6], Edwin J. Ostrin [11], Daniel G. Rosen [12], Junya Fujimoto [1], John V. Heymach [9], Paul Scheet [1,2,5], Steven Dubinett [8], Ignacio I. Wistuba [1], Christopher S. Stevenson [13], Avrum E. Spira [13,14], Linghua Wang [2#], Humam Kadara [1#]

Departments of Translational Molecular Pathology [1], Genomic Medicine [2], Pathology [3], Bioinformatics and Computer Biology [4], Epidemiology [5], Pulmonary Medicine [6], Thoracic, Head and Neck Medical Oncology [9], Cardiovascular and Thoracic Surgery [10] and General Internal Medicine [11], The University of Texas MD Anderson Cancer Center, Houston, TX, USA. Department of Medicine [7], University of Balamand, Koura, Lebanon. Department of Medicine [8], The University of California Los Angeles, Los Angeles, CA, USA. Department of Pathology [10], Nagasaki University Graduate School of Biomedical Sciences, Nagasaki, Japan. Department of Pathology and Immunology [12], Baylor College of Medicine, Houston, TX, USA. Lung Cancer Initiative at Johnson and Johnson [13], Boston, MA, USA. Section of Computational Biomedicine [14], Boston University, Boston, MA, USA.

*: equally contributing co-first authors

#: equally contributing senior co-corresponding authors

bioRxiv preprint doi: https://doi.org/10.1101/2020.09.04.283739; this version posted September 4, 2020. The copyright holder for this preprint (which was not certified by peer review) is the author/funder. All rights reserved. No reuse allowed without permission.

Running title: Spatial single-cell atlas of lung adenocarcinoma

Keywords: lung adenocarcinoma, single-cell RNA sequencing, tumor heterogeneity, spatial evolution, tumor microenvironment.

Financial support: Supported in part by research funding from Johnson and Johnson, National Cancer Institute (NCI) grants R01CA205608, 1U2CCA233238, University of Texas SPORE in Lung Cancer P50CA070907 and P50 core grant CA016672 (ATGC), and NIH grant 1S10OD024977, and the start-up research funds provided to L.W. by U.T. MD Anderson Cancer Center.

Correspondence to: Humam Kadara, Ph.D., Department of Translational Molecular Pathology, The University of Texas MD Anderson Cancer Center. Phone: +1-713-745-3186; Email: hkadara@mdanderson.org or Linghua Wang, M.D., Ph.D., Department of Genomic Medicine, The University of Texas MD Anderson Cancer Center. Phone: +1-713-563-2293; Email: lwang22@mdanderson.org.

Disclosure of conflict of interest: CSS and AES are employees of Johnson and Johnson. HK receives research support from Johnson & Johnson.

bioRxiv preprint doi: https://doi.org/10.1101/2020.09.04.283739; this version posted September 4, 2020. The copyright holder for this preprint (which was not certified by peer review) is the author/funder. All rights reserved. No reuse allowed without permission.

ABSTRACT

Little is known of the geospatial architecture of individual cell populations in lung adenocarcinoma (LUAD) evolution. Here, we perform single-cell RNA sequencing of 186,916 cells from five early-stage LUADs and fourteen multi-region normal lung tissues of defined spatial proximities from the tumors. We show that cellular lineages, states, and transcriptomic features geospatially evolve across normal regions to the LUADs. LUADs exhibit pronounced intratumor cell heterogeneity within single sites and transcriptional lineage-plasticity programs driven by *KRAS* mutations. T regulatory cell phenotypes are increased in normal tissues with closer proximity to LUAD, in contrast to diminished signatures and fractions of cytotoxic CD8+ T cells, antigen-presenting macrophages and inflammatory dendritic cells. Further, the LUAD ecosystem harbors gain of ligand-receptor based interactions involving increased expression of CD24 antigen on epithelial cells and SIGLEC10 on myeloid subsets. These data provide a spatial atlas of LUAD evolution, and a resource for identification of targets for treatment.

Statement of significance: The geospatial ecosystem of the peripheral lung and early-stage LUAD is not known. Our multi-region single-cell sequencing analyses unravel cell populations, states, and phenotypes in the spatial and ecological evolution LUAD from the lung that comprise high-potential targets for early interception.

bioRxiv preprint doi: https://doi.org/10.1101/2020.09.04.283739; this version posted September 4, 2020. The copyright holder for this preprint (which was not certified by peer review) is the author/funder. All rights reserved. No reuse allowed without permission.

INTRODUCTION

Lung adenocarcinoma (LUAD) is the most common histological subtype of lung cancer and accounts for most cancer deaths (1,2) Over the past decade and following results from the National Lung Screening Trial, annual low dose CT screening was endorsed in an effort to reduce lung cancer mortality (3). Since then, an increasing number of early-stage LUAD diagnoses has warranted the need for novel personalized early-treatment strategies, which in turn heavily rests on an improved understanding of the molecular and cellular processes underlying early LUAD development.

Previous studies have identified molecular alterations in histologically normal-appearing epithelial *fields* that are close to solid tumors including those of the lung and that are less prevalent or absent in relatively more distant (from the tumor) regions -- suggesting geospatial heterogeneity in the uninvolved lung that is pertinent to development of a nearby tumor (4). While these studies have provided valuable insights into the *spatial* development of cancer from a particular niche in the lung, they have been mainly guided by bulk profiling approaches (4,5). It is now appreciated that editing of the immune microenvironment towards protumor phenotypes including escape of immune surveillance portends the underlying biology, development, and progression of LUAD (5). Yet, the interplay between individual immune cell populations (and other cell subsets) in spatial development of early-stage LUAD is not known. Technologies that profile tissues at single-cell resolution have permitted delineating the molecular and cellular complexity of tumor ecosystems. Recent reports have employed single-cell sequencing technologies to chart the immune microenvironment of advanced lung cancers as well as to probe mechanisms underlying lung tumor metastasis and response to targeted therapies (6-9). Yet, the complex spatial evolution of heterogeneous cellular populations and their interactions, and as an early-stage LUAD develops from the peripheral lung, has remained largely unresolved.

Here, we sought to discern the spatial atlas of the peripheral lung and early-stage LUAD at single-cell resolution to better understand the topological architecture of LUAD

bioRxiv preprint doi: https://doi.org/10.1101/2020.09.04.283739; this version posted September 4, 2020. The copyright holder for this preprint (which was not certified by peer review) is the author/funder. All rights reserved. No reuse allowed without permission.

evolution. We performed deep scRNA-seq analysis of 19 spatial regions, including enriched epithelial populations, from five early-stage LUADs and 14 multi-region normal-appearing lung tissues with differential and defined spatial proximities from the tumors. Our study unravels tumor evolutionary trajectories as well as geospatial evolution in cell populations, their expression signatures, and ligand-receptor based interactions that portray how early-stage LUAD develops from the lung ecosystem.

RESULTS

Single-cell spatial landscape of early-stage LUAD

To begin to chart a comprehensive single-cell atlas of early-stage LUAD and the peripheral lung, we performed scRNA-seq on all cells from a freshly resected early-stage LUAD (P1) as well as matched tumor-adjacent and relatively more distant normal lung tissues (**Fig. 1A)**. The spatial locations of multi-region normal tissues were carefully defined with respect to the tumor edge (Supplementary Methods), such that the studied samples span a spatial continuum and, thus, enable interrogation of geospatial relationships among early-stage LUAD and the peripheral lung tissues, hereby defined as LUAD “field”. Unsupervised clustering of 15,132 QC-passed cells revealed cell clusters representing 5 major cellular lineages, namely epithelial, endothelial, myeloid, lymphoid, and stromal cell subsets (**Fig. 1B, Supplementary Fig. S1**). Epithelial (*EPCAM*+) cell fractions were 3.7%, 5.4%, and 3.5% for tumor, tumor-adjacent and -distant normal samples, respectively, at an average of 4.2% and in line with previous studies interrogating different subtypes and/or stages of lung cancer ((8,10); **Fig. 1B and C**).

To increase the throughput and to better capture patterns of cellular heterogeneity based on distance from LUADs, in particular within the epithelial lineage, we performed separate scRNA-seq analysis on epithelial (*EPCAM*+) and non-epithelial (*EPCAM*-) single cells enriched from early-stage LUADs of four additional patients (P2-P5, Methods), each with three matching normal lung tissues of defined spatial proximities to

bioRxiv preprint doi: https://doi.org/10.1101/2020.09.04.283739; this version posted September 4, 2020. The copyright holder for this preprint (which was not certified by peer review) is the author/funder. All rights reserved. No reuse allowed without permission.

LUADs: tumor-adjacent, -intermediate and -distant (total of 19 samples and 35 scRNA-seq libraries from P1-P5; **Fig. 1A**). A total of 186,916 cells were retained for subsequent analyses with a median of 1,844 genes detected per cell (**Supplementary Fig. S1A-S1C; Supplementary Table S1**). By single-cell sequencing two separate fractions (*EPCAM*-positive and *EPCAM*-negative), we were able to profile samples markedly enriched with epithelial cells (37.6%, n = 70,030 epithelial cells) in comparison to the unbiased approach (4.2%, non-*EPCAM*-enriched) in P1 (**Fig. 1D**). Cells were uniformly derived from all spatial samples and their lineage cluster fractions spatially distributed along the continuum of LUAD-to-distant normal tissues (**Fig. 1E**). We next computed the Euclidean distance metric and from this inferred hierarchical relationships among major cell lineages across the spatial fields (**Fig. 1F,** see **Methods**). Overall, cells of the LUAD tumor samples were transcriptomically distinct from those of the normal samples across major cell lineages. Of note, we found that cells from adjacent normal samples in 3 out 5 patients (P2, P4 and P5) were clustered more closely with those of LUAD tumor samples (i.e. lymphoid and myeloid lineages) than those of intermediate and distant normal tissues, thereby reflecting possible transcriptomic gradients (**Fig. 1F**).

We then further classified lymphoid and myeloid lineages and determined major cell types, such as T cells, B cells, natural killer (NK) cells, macrophages, or dendritic cells (DC) based on expression of canonical marker genes (**Fig. 1G; Supplementary Fig. S1E, Methods**). Analysis of spatial cell composition revealed distinct topological gradients including greatly increased fractions of B cells and decreased abundance levels of NK cells with greater proximity to the tumors (**Fig. 1H; Supplementary Table S2**), which were evident and consistent across patients (**Fig. 1I**). These observations highlight geospatial transcriptomic heterogeneity in single-cell tumor microenvironment landscape of early-stage LUADs.

Spatial diversity and intratumoral heterogeneity of lung epithelial lineage

We next interrogated spatial epithelial features of the LUADs and multi-region normal tissues. The 70,030 epithelial cells formed 10 distinct clusters representing different airway lineages including alveolar type I (AT1; C2, *AGER*+), AT2 (C3; *SFTPC*+), basal

bioRxiv preprint doi: https://doi.org/10.1101/2020.09.04.283739; this version posted September 4, 2020. The copyright holder for this preprint (which was not certified by peer review) is the author/funder. All rights reserved. No reuse allowed without permission.

(C4; *KRT15*+), bronchioalveolar (C5; *SFTPC*+/*SCGB1A1*+), ciliated (C6; *PIFO*+) and club/secretory (C7; *BPIFB1*+) cells (**Figs. 2A and B; Supplementary Fig. S2A; Supplementary Table S3**). We also identified, as distinct clusters, the recently-described and rare ionocytes (C8; *FOXI1*+/*CFTR*+; (11)), understudied bipotent alveolar progenitors (C1; (12)), as well as unique cell states such as proliferating basal cells (C10; *TOP2A*+). In addition, we noted a cluster of malignant-enriched (C9) cells of mixed lineage (8) mostly from the LUADs (**Fig. 2A-C**). Cells from the five LUADs were predominantly, yet not exclusively, comprised of C9 cells (**Fig. 2B; Supplementary Fig. S2B; Supplementary Table S4**). Interestingly, few cells from the normal tissues were found in the C9 cluster (**Fig. 2A-C)**. Therefore, to distinguish *bona fide* malignant cells from non-malignant subsets, we employed a strategy that infers copy number variations (CNVs) from scRNA-seq data in every epithelial cell (13) (Methods). We found overall high CNV (inferCNV) scores in cells from C9 (**Fig. 2A**, right), thereby supporting the overall malignant assignment of this cluster. We also noted pronounced steady-state enrichment or depletion of epithelial subsets with closer spatial proximity to the tumors (**Fig. 2C and D**). Relative to cells from tumor-intermediate or -distant normal sites, cells from tumor-adjacent normal tissues were, overall, more transcriptomically similar (clustered closely) to those from the LUADs (**Fig. 2E)**, signifying spatial epithelial patterns that are possibly tumor-pertinent.

Alveolar differentiation hierarchies have been shown to partake in lung tumor development *in vivo* (12,14,15). In our cohort, alveolar cells with definitive lineage features (e.g. AT1, AT2, and alveolar progenitors) were marked depleted in LUAD tissues (**Fig. 2C and D)**, which prompted us to dissect potential alveolar differentiation trajectories. Pseudotemporal ordering of alveolar cells revealed a developmental hierarchy that was initiated by AT2 cells and that followed a main trajectory of differentiation into AT1 cells **(Supplementary Fig. S2C and S2D)** in close agreement with previous studies in mice (12,14,15). The differentiation trajectory included increased NOTCH signaling score (**Supplementary Fig. S2E and S2F)** in line with previously reported role of NOTCH in AT2-to-AT1 differentiation and alveolar repair (16).

bioRxiv preprint doi: https://doi.org/10.1101/2020.09.04.283739; this version posted September 4, 2020. The copyright holder for this preprint (which was not certified by peer review) is the author/funder. All rights reserved. No reuse allowed without permission.

To further investigate malignant programs, we performed subclustering of malignant-enriched C9 cells (n = 10,667 cells) while projecting inferCNV scores, which separated likely malignant cells from subsets of normal tissues such as those evident in P2 (**Fig. 2F; Supplementary Fig. S2G; Supplementary Table S5**). We noted overall low inferCNV scores in malignant-enriched cells derived from the LUAD of P2 **(Fig. 2F)**. Interestingly, among all P2 epithelial subsets, 29% of malignant-enriched cells (160 of 547) harbored the *KRAS* G12D mutation (**Fig. 2F and G; Supplementary Fig. S2H**). These cells exhibited distinctively high expression of *MUC5AC* (**Fig. 2G**) and tumor markers (e.g., *CEACAM5*, **Supplementary Fig. S2I; Supplementary Table S6**). They also displayed elevated levels of *LCN2* and reduced expression of *NKX2-1* when compared to *KRAS* wild type cells from the same LUAD (**Supplementary Fig. S2I; Supplementary Table S6**), suggestive of mucinous differentiation (17,18) and in line with the histological (mucinous) pattern of this tumor (**Supplementary Table S1**). These findings underscore spatial heterogeneity dynamics comprising driver mutation, lineage plasticity, and stable chromosomal alterations that are unique to the cellular ecosystem of *KRAS*-mutant LUAD.

Unlike P2, C9 cells in P3 and P5 were almost exclusively derived from the LUAD tissues **(Fig. 2F)**. In P3 LUAD, we identified large-scale chromosomal alterations (**Supplementary Fig. S2G; Supplementary Table S5)**, based on which unsupervised clustering analysis revealed 4 clusters with differential CNV profiles. Among them, three clusters (C2, C3, and C4) exhibited pronounced CNVs that were indicative of malignant cell features (**Fig. 2H**, left**)**. Notably, we found an additional CNV event (i.e. gain of 1p) unique to cells of cluster C4 but not C2 or C3, possibly signifying a late event in the evolutionary trajectory of P3 LUAD. When inferCNV clusters were projected on the pseudotime trajectory plot, we observed a branched differentiation trajectory that mainly started with cells of C2 and C3 and comprised few “normal cells” with club and secretory lineage, and that later branched into cells of inferCNV cluster C4 **(Fig. 2I**, top**)** -- suggesting that P3 LUAD perhaps originated from club/secretory cells and that indeed C4 evolved from C2 and C3. P5 LUAD comprised 6 distinct inferCNV clusters that are

bioRxiv preprint doi: https://doi.org/10.1101/2020.09.04.283739; this version posted September 4, 2020. The copyright holder for this preprint (which was not certified by peer review) is the author/funder. All rights reserved. No reuse allowed without permission.

indicative of high degree of genotypic heterogeneity within the same tumor region **(Fig. 2H**, right**)**. Among these clusters, cells of C1 had more intensive CNVs, while cells of C4 clustered the closest to those of C3 which comprised mostly non-malignant cells **(Fig. 2H**, right**)**. Pseudotime trajectory analysis revealed a C4-to-C1 evolutionary path, which in contrast to P3 was unidirectional and unbranched, suggesting that C4 and C1 in P5 signified malignant cells from early and late developmental states, respectively **(Fig. 2I**, bottom**)**. Together, our single-cell interrogation of a large number of epithelial cells from multi-region tissues identified diverse epithelial identities, developmental malignant trajectories, as well as high resolution intratumor cell heterogeneity.

Lymphoid reprogramming towards a protumor microenvironment

We further characterized lymphoid spatial dynamics **(Fig. 1H and I)**, including unique cellular states across all lymphoid clusters (n = 53,882 cells) in the LUAD field samples (see Methods; **Supplementary Fig. S3A**). This clustering analysis unveiled 10 transcriptomically distinct lymphoid cell types/states **(Fig. 3A and 3B, Supplementary Table S7)** that were, overall, spatially modulated by tumor proximity **(Fig. 3C; Supplementary Fig. S3B)**. Relative to normal tissues, LUADs were heavily enriched with plasma cells *(SDC1+/MZB1+)*, B cells (*CD19+/CD22*+), and regulatory T cells (Treg; *FOXP3*+) **(Fig. 3A-C)**. With increasing tumor proximity, we noted a gradual decrease in NK cells (*GNLY*+), innate lymphoid cells (ILCs), both *GZMA*-hi and *GNLY*-hi CD4+ cytotoxic T lymphocytes (CTL; *CD40LG+, BATF*+), and *GNLY*-hi CD8+ CTLs, all of which were, overall, depleted in the LUADs **(Fig. 3A-C)**.

We further performed subclustering analysis of CD8+ T cells, which revealed 3 subpopulations, naïve CD8+ T cells, *GZMK*-hi CD8+ CTLs, and *GNLY*-hi CD8+ CTLs, with differential expression of cell state signatures (**Fig. 3D; Supplementary Tables S8 and S10).** We also computed the naïve and cytotoxic T cell scores using curated gene signatures of naïve and cytotoxic T cells (see Methods), respectively. Consistently, the naïve CD8+ T cells showed high naïve T cell scores but low cytotoxic T cell scores and were composed of cells across all samples in the LUAD fields. In contrast, the *GNLY*-hi CD8+ CTLs exhibited high expression levels of cytotoxicity genes (*TBX21, KLF3,*

bioRxiv preprint doi: https://doi.org/10.1101/2020.09.04.283739; this version posted September 4, 2020. The copyright holder for this preprint (which was not certified by peer review) is the author/funder. All rights reserved. No reuse allowed without permission.

FCGR3A, KLRG1, *KLRB1*) and high cytotoxic activity but were specifically depleted in LUAD samples of all patients **(Fig. 3C-E).** In line with this, we also observed a significant spatial pattern of reduced cytotoxic activity in P3 and P4 (**Supplementary Fig. S3D).** Overall, CD8+ CTLs showed significant and spatially-modulated reduction in cytotoxic signature score (depleted in tumors of all patients) and decreased expression of major cytotoxicity genes, including reduced *NKG7* and *GNLY* expression levels **(Fig. 3E)**.

Spatial analysis of CD4+ T cell states (**Supplementary Tables S9 and S10**) showed that LUAD tissues were specifically enriched with *FOXP3*+ Tregs **(Fig. 3F and 3G; Supplementary Table S11)** and the Treg signature scores were significantly and spatially increased with closer proximity to all LUADs **(Supplementary Fig. S3E)**. The Tregs cells also expressed high levels of pro-tumor immune checkpoints including *TIGIT, CTLA4, LAG3,* or *PDCD1* (**Fig. 3G**). Of note, the fraction of Tregs co-expressing both *CTLA-4* and *TIGIT* immune checkpoints was progressively higher along the spectrum of distant normal sites to more adjacent (to the tumor) regions up to the LUADs **(Fig. 3G**, bottom**)**. In contrast, we noted a significant reduction of cytotoxic CD4+ CTLs characterized by high expression of *GZMA*, *GNLY*, or both *GZMA* and *GZMH*, with increasing proximity to all LUADs **(Supplementary Fig. S3F-H)**.

We further examined the spatial enrichment of LUADs with plasma cells and B cells **(Fig. 3A-C; Supplementary Table S11).** Expression profiling of plasma cells revealed spatial changes in isotype-switching, such as increased *IGHA1/2* and decreased *IGHG1/3* with increasing proximity to P3 and P5 LUADs **(Supplementary Fig. S3I-K; Supplementary Table S12)**. Based on differential gene expression profiles, we identified 3 distinct subsets of B cell states **(Supplementary Table S13)**, including a LUAD-enriched subcluster (C0) with high expression levels of *RAC2*+ and *ACTG*+ **(Supplementary Fig. S3L-N)**, that are known to play key roles in synapse formation in B cells (19). Importantly, when analyzed in an external cohort of matched normal lung, preneoplasia and LUAD (20), the B cell signature (C0) was progressively increased across atypical adenomatous hyperplasias (AAH), the preneoplastic precursors of

bioRxiv preprint doi: https://doi.org/10.1101/2020.09.04.283739; this version posted September 4, 2020. The copyright holder for this preprint (which was not certified by peer review) is the author/funder. All rights reserved. No reuse allowed without permission.

LUAD, and invasive LUAD lesions compared to matched normal lung tissues **(Supplementary Fig. S3O).** Taken together, these analyses propose spatial properties in lymphoid cell states that underlie pro-tumor immune remodeling in early-stage LUAD.

Depletion of antigen presenting macrophages and inflammatory dendritic cells

Spatial LUAD field patterns in myeloid cells **(Fig. 1H and 1I)** prompted us to further investigate myeloid subsets and cellular states in the early-stage LUADs and their normal multi-region tissues **(Supplementary Fig. S4A)**. In total, 45,803 myeloid cells were clustered into 13 distinct subsets: classical monocytes (*S100A8+, S100A9+*), non-classical monocytes *(CDKN1C+*), mast cells *(MS4A2+)*, neutrophils (*IL1A+*), M2-like macrophages C1 (*TREM2+)*, M2-like macrophages C5 (*CD163+*), alveolar macrophages (*MARCO+)*, classical dendritic cells 1 (cDC1; *CLEC9A+*), cDC2 (*CLEC10A+*), plasmacytoid DC (pDC; *PLD4+*), other DCs (*CCL22+)* and proliferating myeloid cells *(TOP2A+)* **(Fig. 4A and 4B; Supplementary Tables S14 and S15)**. Mapped to the field samples, M2-like macrophages C5, monocytes (classical and non-classical), and mast cells were gradually depleted with increasing tumor proximity, whereas M2-like macrophages C1, proliferating myeloid subsets and cDC2 cells were steadily enriched in the tumors **(Fig. 4A and 4C; Supplementary Fig. S4B and S4C).**

We next performed subclustering analysis of monocytes and macrophages (n = 27,664 cells) which revealed five distinct subclusters, and confirmed the unique enrichment of M2-like macrophages C1 in the LUAD tissues **(Fig. 4D; Supplementary Tables S14)**. Further, we characterized monocyte and macrophage subsets by antigen presentation capability (i.e. antigen presentation signature score), and found that the M2-like macrophages C1 showed diminished antigen presentation scores compared to cells of M2-like macrophages C5 which were mainly enriched in normal samples **(Fig. 4D; Supplementary Table S16)**. In addition, we interrogated the spatial expression of antigen presentation-related genes in this cluster. We found markedly reduced expression levels of antigen presentation signature genes, including MHC class I and MHC class II members with increasing spatial proximity to the LUADs **(Fig. 4E and 4F)**. Furthermore, the spatially-driven pattern of macrophage antigen presentation depletion

bioRxiv preprint doi: https://doi.org/10.1101/2020.09.04.283739; this version posted September 4, 2020. The copyright holder for this preprint (which was not certified by peer review) is the author/funder. All rights reserved. No reuse allowed without permission.

was evident across M2-like macrophages combined from both clusters C1 and C5 and was statistically significant in 4 of the 5 LUAD patient fields **(Fig. 4G)**.

To characterize spatial DC dynamics in early-stage LUAD with respect to cellular states, we first examined gene and signature score differences between different subsets of DCs (n = 8,694). Spatial field patterns were evident in cDC2 and pDC subsets **(Fig. 4H)**. We observed differential expression of an inflammatory gene signature between the three cDC2 subclusters with C1, cells of which exhibited the lowest inflammatory scores, heavily enriched in the LUADs **(Fig. 4I and 4J)**. In addition, unsupervised subclustering analysis of cDC2 cells using a different approach (SC3, see Methods) identified three distinct cDC2 subclusters, characterized by differential expression of the chronic inflammatory gene signature (highly enriched in C2) and MHC class II genes (enriched in C0/1) **(Supplementary Fig. S4D; Supplementary Table S17)** that were previously shown to discriminate inflammatory from non-inflammatory cDCs (21). Reduced expression of pro-inflammatory genes and increased expression of anti-inflammatory genes was evident in all cDC2 cells along the continuum of normal-to-LUAD space **(Fig. 4K).** cDC2 subcluster with the highest inflammatory score (C2) was markedly under-represented in the LUADs and was further characterized by a spatially diluted inflammatory signature score with increasing tumor proximity **(Fig. 4L and 4M**). Notably, the inflammatory signature score significantly and progressively decreased along the continuum from normal lung tissues, to matched premalignant AAHs and invasive LUADs (**Fig. 4N**) in sharp contrast to non-inflammatory DC expression components **(Supplementary Fig. S4E).** We also studied pDC subsets and found spatial enrichment of *FOS, FOSB,* and *JUN* with increasing proximity to the tumors **(Supplementary Fig. S4F and S4G)**. Altogether, these data describe spatial immune remodeling dynamics comprising gradual loss of antigen presentation in macrophage subclusters and of inflammatory phenotypes in subsets of DCs in early-LUAD microenvironment.

We also identified multiple stromal populations in our dataset **(Supplementary Fig. S5A-S5C)**, including tumor enrichment of vascular and airway smooth muscle cells,

bioRxiv preprint doi: https://doi.org/10.1101/2020.09.04.283739; this version posted September 4, 2020. The copyright holder for this preprint (which was not certified by peer review) is the author/funder. All rights reserved. No reuse allowed without permission.

adventitial fibroblasts C5, and endothelial cell (EC) venule clusters **(Supplementary Fig. S5D and S5E)**. We pinpointed significantly differentially expressed gene sets in the EC venule subpopulation and altered stromal signatures **(Supplementary Fig. S5F)** that support the observed immune-related changes in the LUAD field, and that are in line with previous observations in a cohort of lung cancers of multiple subtypes (10). These comprised tumor-specific activation of extracellular matrix reorganization, syndecan-2 pathway, and neutrophil degranulation, as well as decreased JAK-STAT signaling and reduced antigen-processing cross-presentation **(Supplementary Fig. S5G and S5H)**.

Ligand-receptor based cell-cell communication networks

Crosstalk between tumor cells and elements in the tumor microenvironment, such as immune cells, has been implicated in the progression of solid tumors largely in part by mediating immune-evasive and pro-tumor phenotypes (22). To profile cell-cell communication networks in early-stage LUAD space, we utilized iTALK (23) to leverage signals from our scRNA-seq dataset and visualize ligand-receptor (L-R)-mediated intercellular cross-talk that is spatially modulated within the tumor microenvironment **(Fig. 5A; Supplementary Table S18)**. Computational analysis and annotation were carried out using the iTALK's built-in database focusing on immune checkpoint-receptor pairs (n = 55) and cytokine-receptor pairs (n = 327) **(Fig. 5A)**. Overall, we found reduced overlap of L-R interactions between the tumor and distance normal tissues than that between the tumor and more proximal (adjacent, intermediate) regions (**Fig. 5B**).

By comparative analysis, we identified altered cellular interactions that were significantly and differentially increased or decreased in LUADs *versus* their respective spatial normal tissues (**Fig. 5C; Supplementary Fig. S6A)**. Specifically, we noted increased interactions between immune checkpoint proteins *CD24* or *LGALS9 (Galectin-9)* on tumor epithelial cells, and *SIGLEC10* on macrophages or *HAVCR2 (TIM-3)* on DCs, respectively, and which were shared across multiple patients (**Fig. 5C and 5D**; **Supplementary Fig. S6A and S6B; Supplementary Table S19)**. These interactions

bioRxiv preprint doi: https://doi.org/10.1101/2020.09.04.283739; this version posted September 4, 2020. The copyright holder for this preprint (which was not certified by peer review) is the author/funder. All rights reserved. No reuse allowed without permission.

were differentially enriched in tumors *versus* normal tissues at different distances from the tumor **(Fig. 5C; Supplementary Fig. S6A)**. Expression levels of the checkpoints *CD24* and *LGALS9 (Galectin-9)* were increased in epithelial cells from LUAD tissues in general, and in malignant epithelial cells in particular, and accompanied by increased expression of their cognate predicted ligands *SIGLEC10* and *HAVCR2 (TIM-3)*, respectively, on myeloid cells and with increasing tumor proximity (**Fig. 5D; Supplementary Fig. S6B).** These interactions suggest a spatial pattern of modulation in cell-cell communication that is mediated by epithelial inhibitory checkpoint signaling to myeloid cells. Targeted analysis of *CD24* expression in an external cohort using the Nanostring platform revealed progressively and markedly increased expression of the antigen across normal lung tissues, AAHs, and LUADs **(Fig. 5F)**. *CD24* positively correlated with expression of the epithelial marker *EPCAM* as well as with levels of pro-tumor and immune suppressive features (*TIGIT, CTLA4, FOXP3, CCL19*)**,** in contrast to negatively correlating with anti-tumor immune markers (*GZMB, GZMH, PRF1*) **(Fig. 5F; Supplementary Fig. S6G).** These pro-tumor and epithelial patterns of *CD24* were further validated in LUADs (n = 51) from The Cancer Genome Atlas (TCGA) cohort (24) compared to matched adjacent normal lung tissues **(Fig. 5G and 5H; Supplementary Fig. S6H)**, thereby suggesting a potential role for epithelial *CD24* signaling in pro-tumor immune reprogramming in LUAD evolution.

We also identified cytokine-receptor pairs that were differentially modulated in the LUAD space, such as communication between tumor epithelial cells with high expression of the cytokine *CX3CL1*, and DCs or macrophages expressing increased levels of its cognate receptor *CX3CR1* **(Supplementary Fig. S6C, S6D, S6E, S6F; Supplementary Table S18)**. *CX3CR1* was increasingly expressed on macrophages and DCs but decreased on CD8 T cells of tumor samples **(Fig. 5F)**, in line with previous reports implicating macrophage *CX3CR1* with pro-tumor features (25). These findings signify a potential spatial enrichment of pro-tumorigenic and tumor-mediated cytokine signaling to macrophages infiltrating the LUAD space.

bioRxiv preprint doi: https://doi.org/10.1101/2020.09.04.283739; this version posted September 4, 2020. The copyright holder for this preprint (which was not certified by peer review) is the author/funder. All rights reserved. No reuse allowed without permission.

DISCUSSION

Previously, spatial molecular changes have been documented in the local niche of LUAD including loss-of-heterozygosity in 3p and 9p, point mutations and tumor suppressor methylation (26,27). Earlier work also underscored transcriptome profiles, somatic driver variants, as well as genome-wide allelic imbalance that are shared between lung cancer and adjacent normal-appearing airway cells but that are absent in distant normal cells, thereby pointing to putative drivers of lung oncogenesis (4,5). As such, the interrogation of spatial dynamics in LUADs has been a topic of interest, particularly owing to its utility as a surrogate for studying difficult-to-obtain longitudinal patient (including precursor) samples. However, much of these studies have focused on understanding, by bulk profiling methods, spatiotemporal profiles in an aggregate of cells, thereby inadvertently obscuring the individual contributions of epithelial and tumor microenvironmental cues to the pathogenesis of lung cancer. Our knowledge of the spatial architecture of individual cell populations in the evolution of this malignancy remains poorly understood. By single-cell interrogation of multi-region samples, we here characterized spatial and ecological maps comprising many epithelial and non-epithelial subsets and underlying emergence of early-stage LUAD from its local niche.

Multi-region or spatial analyses have been employed to interrogate intratumor heterogeneity (ITH) in solid tumors including LUADs, in order to understand evolutionary trajectories and therapy response (28). Cohorts based on multi-region sampling and microdissection strategies have increased the resolution for detecting subtle, rare and subclonal events by bulk sequencing approaches. Our analyses here showed that ITH is evident at the tumor epithelial cell and intra-site level, i.e. within the same tumor region or tissue. We applied an integrative approach to dissect ITH of malignant cells and characterized cell clusters with differential transcriptomic profiles, evolution trajectories, CNV burdens, and/or driver mutations. We also found “normal” cells in the LUAD tissues themselves that are close in the inferred trajectory paths to specific malignant cell subsets (e.g. club/secretory cells for the mucinous LUAD in P2) and perhaps represent the cells-of-origin for tumor cells. It is noteworthy that we found

bioRxiv preprint doi: https://doi.org/10.1101/2020.09.04.283739; this version posted September 4, 2020. The copyright holder for this preprint (which was not certified by peer review) is the author/funder. All rights reserved. No reuse allowed without permission.

in the normal-appearing samples cells with features of malignant-enriched subsets and demonstrating heterogeneous CNV profiles. Whether these cells comprise early LUAD precursors, mutagenic clones that do not progress to malignancy (e.g. negatively selected by the immune microenvironment), or putative molecular field cancerization remains to be investigated. It is important to mention that LUAD exhibits remarkable inter-patient heterogeneity in histological differentiation patterns, driver alterations and suggested tumor cells-of-origin (29). We could not characterize the full spectrum in the heterogeneity of these features (e.g., programs in tumor cells-of-origin of different lineages) given the limited number of patients profiled. Nonetheless, our in-depth analysis of a relatively large number of epithelial cells unveiled different characteristics (airway lineage trajectories, malignant cell programs, potential tumor cells-of-origin, and cellular ITH) of the epithelial architecture of early-stage LUAD development that could be extended in the future to a larger and more diverse array of LUADs.

We pinpointed G12D mutations in *KRAS*, the most frequently mutated oncogene in LUAD, to a unique subset of malignant cells within P2 tumor. These cells had overall low copy number alterations, perhaps reminiscent of findings in LUADs driven by strong driver genes *in vivo* (30). These cells comprised increased expression of genes associated with *KRAS*-mutant cancer such as *LCN2* which is a marker of inflammation (17,31) and elevated levels of genes associated with hyper-mutation such as *CDA* (32). *KRAS*-mutant cells, compared to other malignant-enriched cells from P2, exhibited reduced expression of the lineage-specific oncogene *NKX2-1* (33). Earlier studies demonstrated that increased LCN2 and reduced NKX2-1 is observed in mucinous *KRAS*-mutant LUADs or those undergoing gastric differentiation (17,18), which is in line with the histological variant of P2 LUAD. It is noteworthy that *NKX2-1* exhibits context-dependent roles in LUAD development. While Nkx2-1 was shown to enhance *Egfr*-driven lung tumorigenesis (34), Winslow et al demonstrated that the transcription factor suppresses *Kras*-mutant LUAD by controlling tumor differentiation as well as limiting progression and metastatic potential (35). This is in line with our finding of reduced expression of airway lineage-specific genes (e.g. *SCGB3A1*, *SFTPB*) suggestive of loss of differentiation in the *KRAS*-mutant cells compared to other malignant-enriched cell

bioRxiv preprint doi: https://doi.org/10.1101/2020.09.04.283739; this version posted September 4, 2020. The copyright holder for this preprint (which was not certified by peer review) is the author/funder. All rights reserved. No reuse allowed without permission.

subclusters from the same LUAD tissue. Our observations are also in accordance with the acquisition of a mixed-lineage phenotype by malignant lung epithelial cells recently reported by Laughney and colleagues (8). Our findings also allude to the possibility that tumor cell lineage plasticity may occur at the early stage of *KRAS*-mutant LUAD carcinogenesis – a supposition that can be better explored with sequencing of a larger and more diverse repertoire of *KRAS*-mutant cells.

Earlier studies have shown that immunosuppressive T regulatory cells are crucial for immune evasion in lung cancer (36,37). By single-cell analysis of diverse lymphoid subsets, we found Tregs co-expressing both *TIGIT* and *CTLA-4* immune checkpoints and that were progressively enriched with increasing geospatial proximity to the LUADs – suggesting a value in combinatorial targeting of multiple checkpoints for immunotherapy of early-stage LUAD. We pinpointed B cell signatures implicated in actin remodeling and immunological synapse formation that are spatially enriched in the LUADs and progressively increased along the course of normal to preneoplasia and invasive LUAD. These data suggest important yet unexplored roles for B cell phenotypes in immune evolution of LUAD. Our spatial single-cell analysis also pointed to mechanisms by which the myeloid immune microenvironment permits LUAD pathogenesis. Our interrogation of macrophage subsets revealed downregulation/loss of antigen presentation in tumor-specific M2-like macrophages, whereby expression levels of MHC genes as well as genes involved in peptide transport and loading (*TAP1, TAP2, TAPBP;* (38)) were markedly reduced. Our study also unveiled relatively understudied immune subsets in LUAD. We found DC subclusters and programs that were recently reported in other sites (21), including a non-inflammatory cDC signature with higher expression of MHC class II genes and that is enriched in LUAD relative to matched preneoplastic or normal tissues, thereby possibly informing of immune cues that could be harnessed to manipulate the immunogenicity of tumors. We also identified an inflammatory tumor-depleted cDC cluster with increased expression of *CD163*, *CD36*, *CD14*, *S100A9*, and *S100A8*. Interestingly, dendritic CD36 is a scavenger for the acquisition and presentation of cell surface antigens and subsequent sculpting of the Treg repertoire (39), yet the precise consequences of its stark absence in a LUAD-

bioRxiv preprint doi: https://doi.org/10.1101/2020.09.04.283739; this version posted September 4, 2020. The copyright holder for this preprint (which was not certified by peer review) is the author/funder. All rights reserved. No reuse allowed without permission.

specific cDC subset and the effect(s) on the tumor immune microenvironment warrant further investigation. Nevertheless, these findings, along with our observation of decreased expression of the inflammatory DC signature across normal lung to premalignant AAH up to LUAD, suggest that unique cDC subsets play critical roles in LUAD pathogenesis and, thus, could be potential targets for immune-based interception.

Ligand-receptor mediated interactions are known to be the main forms of interactions responsible for cellular signaling mechanisms and cell-to-cell communication, which is especially important during carcinogenesis and immune response (22). A better understanding of cell-to-cell communication networks, particularly ligand-receptor mediated interactions, may help elucidate tumor-immune co-evolution and immune reprogramming, and thus, help identify potential therapeutic targets. However, this has been hampered by the lack of bioinformatics tools for efficient data analysis and visualization. In this study, we applied the iTALK tool (23) developed by our group and performed a deep analysis of cellular interaction networks. We identified significant immune checkpoint- (e.g. *CD24*, *Galectin-9*, or *TIM-3)* and cytokine- (e.g. *CX3CL1)* receptor interactions whose enrichment or depletion in the LUAD space signified a highly pro-tumorigenic milieu. These findings are in accordance with the CD24–Siglec-10 interaction and subsequent “do not eat me” signal recently highlighted in breast cancer (40). Additionally, our findings of prominently increased expression of *CD24* in hyperplastic precursors (AAH) and LUADs compared to normal lung, and its association with pro-tumor and immunosuppressive phenotypes in this pathologic continuum, propose immune functions for CD24 in lung cancer that extend beyond its prognostic role (41) and that can be harnessed for early intervention. Overall, our interactome analyses implicate novel or understudied immune subsets as culprits in LUAD pathogenesis and provide a rationale for expanding the armamentarium of immune-based cancer therapies.

In summary, our results provide a spatial atlas of early-stage LUAD and its nearby and distant lung ecosystem. This atlas comprises high cellular heterogeneity as well as

bioRxiv preprint doi: https://doi.org/10.1101/2020.09.04.283739; this version posted September 4, 2020. The copyright holder for this preprint (which was not certified by peer review) is the author/funder. All rights reserved. No reuse allowed without permission.

spatial dynamics in cell populations, cell states and their transcriptomic features that underlie evolution of the LUAD from the peripheral lung ecosystem. Our extensive transcriptomic dataset of lung epithelial and immune cells, other populations such as stromal and endothelial subsets, as well as of tumor-pertinent cell-cell interactions constitutes a valuable resource to functionally interrogate LUAD trajectories at high resolution and generate strategies for its early treatment. Also, our study's multi-region sampling design in conjunction with single-cell analysis could help address specific questions in early malignant and immune biology of other solid tumors.

METHODS

Additional description of methods can be found in the Supplementary Data file.

Multi-region sampling of surgically resected LUADs and spatial normal lung tissue specimens

Patients undergoing surgical resection for primary early-stage lung adenocarcinoma (I-IIIA) and who had not received any preoperative therapy were carefully selected for derivation of multi-region samples for single cell analysis (**Supplementary Table S1**). All patients were evaluated at the University of Texas MD Anderson Cancer Center and had provided informed consents under approved institutional review board protocols. Immediately following surgery, resected tissues were processed on ice by an experienced pathologist assistant (PB). One side of the specimen was documented and measured, followed by identification of tumor margin, mapping defined collection sites in one direction along the length of the specimen and spanning the entire lobe, and making incisions into the surface of the lobe for specimen collection according to the following criteria. Based on the placement of the tumor within the specimen, tumor-adjacent and -distant normal parenchyma specimen were assigned at 0.5 cm from the tumor edge and from the periphery of the overall specimen/lobe (furthest distance from the tumor), respectively. An additional tumor-intermediate normal tissue was selected for P2-5 that ranged between 3-5 cm from the edge of the tumor. Sample collection was initiated at normal lung tissues that are farthest from the tumor moving inwards towards

bioRxiv preprint doi: https://doi.org/10.1101/2020.09.04.283739; this version posted September 4, 2020. The copyright holder for this preprint (which was not certified by peer review) is the author/funder. All rights reserved. No reuse allowed without permission.

the tumor to minimize cross-contamination during collection, with each sample being immediately placed in ice-cold RPMI medium supplemented with 2% fetal bovine serum, and transported to the processing lab on ice.

Single cell derivation and scRNA-seq processing

Tumor and spatial normal parenchyma tissues (n = 19 samples) were immediately minced and enzymatically digested, as previously described ((42), Supplementary Data). Following red blood cell removal, cells were filtered and counted. Cells were sorted (by FACS) for viable singlets cells (and also EPCAM+/- fractions from P2-P5). Sorted fractions were then loaded on individual channels of 10X Chromium Microfluidic chips, targeting up to 10,000 cells per fraction. Gene expression libraries were generated according to manufacturer's instructions using Chromium Next GEM Single Cell 5' Gel Bead Kit v1.1 (1000169, 10X Genomics), and sequenced on Illumina NovaSeq 6000 platform (Supplementary Data).

scRNA-seq data analysis

Single-cell analyses were performed using available computational framework. Raw scRNA-seq data were pre-processed, demultiplexed, aligned to human GRCh38 reference and feature-barcodes generated using CellRanger (10X Genomics, version 3.0.2). Details of quality control including quality check, data filtering, identification and removal of cellular debris, doublets and multiplets, batch effect evaluation and correction are found in Supplementary Methods. Following quality filtering, a total of 186,916 cells were retained for downstream analysis. Raw unique molecular identifier (UMI) counts were log normalized and used for principal component analysis using Seurat (43). The output was then processed by Harmony (44) for batch effect correction, followed by unsupervised clustering analysis using Seurat (43). Uniform Manifold Approximation and Projection (UMAP) clustering (45) was used for visualization. *EPCAM*+ cells were partitioned into major airway lineage clusters, followed by subclustering within each compartment/lineage to identify subpopulations. In addition, we applied single-cell consensus clustering (SC3) approach (46) for unsupervised

bioRxiv preprint doi: https://doi.org/10.1101/2020.09.04.283739; this version posted September 4, 2020. The copyright holder for this preprint (which was not certified by peer review) is the author/funder. All rights reserved. No reuse allowed without permission.

clustering analysis. SC3 was run with default parameters and independent of cell lineage annotation. Differentially expressed genes (DEGs) for each cell cluster were identified using the *FindAllMarkers* function in Seurat R package. We applied an integrative approach to define the cell type and determine its functional state of each cluster, based on the enrichment of canonical marker genes, top-ranked DEGs in each cell cluster, and the global cluster distribution, as previously described (47). For transcriptional signature analysis, single-sample GSVA (ssGSVA) was applied to the scRNA-seq data and pathway scores were calculated for each cell using gsva function in GSVA software package (48).

To study hierarchical relationships among cell types identified in this study, pairwise Spearman correlations were calculated from average expression level (*Seurat* function *AverageExpression*) of each cell type, based on which Euclidean distances between cell types were calculated. Unsupervised hierarchical cluster analysis was performed using the R function *hclust*, and the dendrogram was drawn using R package dendextend. Monocle 2 (version 2.10.1) (49) was applied to construct single-cell trajectories. The tool inferCNV (https://github.com/broadinstitute/inferCNV) was applied to infer large-scale CNVs from scRNA-seq data using NK cells from the same dataset as a control. Malignant cells were distinguished from non-malignant subsets based on information integrated from multiple sources including cluster distribution of the cells, marker genes expression, inferred large-scale CNVs, and presence of the *KRAS* mutation. For single-cell somatic *KRAS* mutation analysis, the reads were extracted from the original BAM files using cell-specific barcodes and genomic coordinates of *KRAS* hot spot mutations and then subjected to quality filtering and duplicates removal, followed by mutation identification and annotation. Extracted alignments were manually evaluated using IGV (50). To identify significant ligand-receptor pairs among major cell lineages (CD4 T cells, CD8 T cells, B cells, macrophages, dendritic cells, endothelial cells, epithelial cells and fibroblasts), the top 30% of most highly expressed genes were included in the analysis. Significant cellular interactions were identified using iTALK as previously described (23). For ligand-receptor annotation, the iTALK built-in ligand-receptor database was used.

bioRxiv preprint doi: https://doi.org/10.1101/2020.09.04.283739; this version posted September 4, 2020. The copyright holder for this preprint (which was not certified by peer review) is the author/funder. All rights reserved. No reuse allowed without permission.

Statistical analysis

In addition to the bioinformatics approaches described above for scRNA-seq data analysis, all other statistical analyses were performed using R package v3.6.0. Pseudo-bulk gene expression values for defined cell clusters were calculated by taking mean expression of each gene across all cells in a specific cluster. Pearson's correlation analysis was used to identify genes significantly correlated with *CD24* expression. All statistical significance testing was two-sided, and results were considered statistically significant at p - value < 0.05. The Benjamini-Hochberg method was applied to control the false discovery rate (FDR) in multiple comparisons and to calculate adjusted p - value (q-values).

Data Availability

All sequencing data generated in this study will be deposited in the Gene Expression Omnibus.

bioRxiv preprint doi: https://doi.org/10.1101/2020.09.04.283739; this version posted September 4, 2020. The copyright holder for this preprint (which was not certified by peer review) is the author/funder. All rights reserved. No reuse allowed without permission.

REFERENCES

1. Siegel RL, Miller KD, Jemal A. Cancer statistics, 2018. CA: a cancer journal for clinicians **2018**;68(1):7-30 doi 10.3322/caac.21442.
2. Goldstraw P, Ball D, Jett JR, Le Chevalier T, Lim E, Nicholson AG*, et al.* Non-small-cell lung cancer. Lancet (London, England) **2011**;378(9804):1727-40 doi 10.1016/s0140-6736(10)62101-0.
3. Aberle DR, Adams AM, Berg CD, Black WC, Clapp JD, Fagerstrom RM*, et al.* Reduced lung-cancer mortality with low-dose computed tomographic screening. The New England journal of medicine **2011**;365(5):395-409 doi 10.1056/NEJMoa1102873.
4. Abbosh C, Venkatesan S, Janes SM, Fitzgerald RC, Swanton C. Evolutionary dynamics in pre-invasive neoplasia. Current opinion in systems biology **2017**;2:1-8 doi 10.1016/j.coisb.2017.02.009.
5. Saab S, Zalzale H, Rahal Z, Khalifeh Y, Sinjab A, Kadara H. Insights Into Lung Cancer Immune-Based Biology, Prevention, and Treatment. Front Immunol **2020**;11:159 doi 10.3389/fimmu.2020.00159.
6. Maynard A, McCoach CE, Rotow JK, Harris L, Haderk F, Kerr DL*, et al.* Therapy-Induced Evolution of Human Lung Cancer Revealed by Single-Cell RNA Sequencing. Cell **2020** doi https://doi.org/10.1016/j.cell.2020.07.017.
7. Lavin Y, Kobayashi S, Leader A, Amir ED, Elefant N, Bigenwald C*, et al.* Innate Immune Landscape in Early Lung Adenocarcinoma by Paired Single-Cell Analyses. Cell **2017**;169(4):750-65.e17 doi 10.1016/j.cell.2017.04.014.
8. Laughney AM, Hu J, Campbell NR, Bakhoum SF, Setty M, Lavallée V-P*, et al.* Regenerative lineages and immune-mediated pruning in lung cancer metastasis. Nature Medicine **2020**;26(2):259-69 doi 10.1038/s41591-019-0750-6.
9. Kim N, Kim HK, Lee K, Hong Y, Cho JH, Choi JW*, et al.* Single-cell RNA sequencing demonstrates the molecular and cellular reprogramming of metastatic lung adenocarcinoma. Nature Communications **2020**;11(1):2285 doi 10.1038/s41467-020-16164-1.
10. Lambrechts D, Wauters E, Boeckx B, Aibar S, Nittner D, Burton O*, et al.* Phenotype molding of stromal cells in the lung tumor microenvironment. Nature Medicine **2018**;24(8):1277-89 doi 10.1038/s41591-018-0096-5.
11. Plasschaert LW, Žilionis R, Choo-Wing R, Savova V, Knehr J, Roma G*, et al.* A single-cell atlas of the airway epithelium reveals the CFTR-rich pulmonary ionocyte. Nature **2018**;560(7718):377-81 doi 10.1038/s41586-018-0394-6.
12. Treutlein B, Brownfield DG, Wu AR, Neff NF, Mantalas GL, Espinoza FH*, et al.* Reconstructing lineage hierarchies of the distal lung epithelium using single-cell RNA-seq. Nature **2014**;509(7500):371-5 doi 10.1038/nature13173.
13. Tirosh I, Venteicher AS, Hebert C, Escalante LE, Patel AP, Yizhak K*, et al.* Single-cell RNA-seq supports a developmental hierarchy in human oligodendroglioma. Nature **2016**;539(7628):309-13 doi 10.1038/nature20123.
14. Little DR, Gerner-Mauro KN, Flodby P, Crandall ED, Borok Z, Akiyama H*, et al.* Transcriptional control of lung alveolar type 1 cell development and maintenance

bioRxiv preprint doi: https://doi.org/10.1101/2020.09.04.283739; this version posted September 4, 2020. The copyright holder for this preprint (which was not certified by peer review) is the author/funder. All rights reserved. No reuse allowed without permission.

by NK homeobox 2-1. Proc Natl Acad Sci U S A **2019**;116(41):20545-55 doi 10.1073/pnas.1906663116.

15. Desai TJ, Brownfield DG, Krasnow MA. Alveolar progenitor and stem cells in lung development, renewal and cancer. Nature **2014**;507(7491):190-4 doi 10.1038/nature12930.
16. Finn J, Sottoriva K, Pajcini KV, Kitajewski JK, Chen C, Zhang W*, et al.* Dlk1-Mediated Temporal Regulation of Notch Signaling Is Required for Differentiation of Alveolar Type II to Type I Cells during Repair. Cell Rep **2019**;26(11):2942-54.e5 doi 10.1016/j.celrep.2019.02.046.
17. Treekitkarnmongkol W, Hassane M, Sinjab A, Chang K, Hara K, Rahal Z*, et al.* Augmented Lipocalin-2 is Associated with COPD and Counteracts Lung Adenocarcinoma Development. Am J Respir Crit Care Med **2020** doi 10.1164/rccm.202004-1079OC.
18. Skoulidis F, Byers LA, Diao L, Papadimitrakopoulou VA, Tong P, Izzo J*, et al.* Co-occurring genomic alterations define major subsets of KRAS-mutant lung adenocarcinoma with distinct biology, immune profiles, and therapeutic vulnerabilities. Cancer Discov **2015**;5(8):860-77 doi 10.1158/2159-8290.CD-14-1236.
19. Arana E, Vehlow A, Harwood NE, Vigorito E, Henderson R, Turner M*, et al.* Activation of the small GTPase Rac2 via the B cell receptor regulates B cell adhesion and immunological-synapse formation. Immunity **2008**;28(1):88-99 doi 10.1016/j.immuni.2007.12.003.
20. Sivakumar S, Lucas FAS, McDowell TL, Lang W, Xu L, Fujimoto J*, et al.* Genomic Landscape of Atypical Adenomatous Hyperplasia Reveals Divergent Modes to Lung Adenocarcinoma. Cancer research **2017**;77(22):6119-30 doi 10.1158/0008-5472.Can-17-1605.
21. Villani AC, Satija R, Reynolds G, Sarkizova S, Shekhar K, Fletcher J*, et al.* Single-cell RNA-seq reveals new types of human blood dendritic cells, monocytes, and progenitors. Science (New York, NY) **2017**;356(6335) doi 10.1126/science.aah4573.
22. Maman S, Witz IP. A history of exploring cancer in context. Nat Rev Cancer **2018**;18(6):359-76 doi 10.1038/s41568-018-0006-7.
23. Wang Y, Wang R, Zhang S, Song S, Jiang C, Han G*, et al.* iTALK: an R Package to Characterize and Illustrate Intercellular Communication. bioRxiv **2019**:507871 doi 10.1101/507871.
24. Cancer Genome Atlas Research N. Comprehensive molecular profiling of lung adenocarcinoma. Nature **2014**;511(7511):543-50 doi 10.1038/nature13385.
25. Schmall A, Al-Tamari HM, Herold S, Kampschulte M, Weigert A, Wietelmann A*, et al.* Macrophage and cancer cell cross-talk via CCR2 and CX3CR1 is a fundamental mechanism driving lung cancer. Am J Respir Crit Care Med **2015**;191(4):437-47 doi 10.1164/rccm.201406-1137OC.
26. Belinsky SA, Palmisano WA, Gilliland FD, Crooks LA, Divine KK, Winters SA*, et al.* Aberrant promoter methylation in bronchial epithelium and sputum from current and former smokers. Cancer Res **2002**;62(8):2370-7.

bioRxiv preprint doi: https://doi.org/10.1101/2020.09.04.283739; this version posted September 4, 2020. The copyright holder for this preprint (which was not certified by peer review) is the author/funder. All rights reserved. No reuse allowed without permission.

27. Powell CA, Klares S, O'Connor G, Brody JS. Loss of heterozygosity in epithelial cells obtained by bronchial brushing: clinical utility in lung cancer. Clin Cancer Res **1999**;5(8):2025-34.
28. Zhang J, Fujimoto J, Zhang J, Wedge DC, Song X, Zhang J*, et al.* Intratumor heterogeneity in localized lung adenocarcinomas delineated by multiregion sequencing. Science **2014**;346(6206):256-9 doi 10.1126/science.1256930.
29. Chen Z, Fillmore CM, Hammerman PS, Kim CF, Wong K-K. Non-small-cell lung cancers: a heterogeneous set of diseases. Nature reviews Cancer **2014**;14(8):535-46 doi 10.1038/nrc3775.
30. McFadden DG, Politi K, Bhutkar A, Chen FK, Song X, Pirun M*, et al.* Mutational landscape of EGFR-, MYC-, and Kras-driven genetically engineered mouse models of lung adenocarcinoma. Proceedings of the National Academy of Sciences of the United States of America **2016**;113(42):E6409-E17 doi 10.1073/pnas.1613601113.
31. Moschen AR, Gerner RR, Wang J, Klepsch V, Adolph TE, Reider SJ*, et al.* Lipocalin 2 Protects from Inflammation and Tumorigenesis Associated with Gut Microbiota Alterations. Cell Host Microbe **2016**;19(4):455-69 doi 10.1016/j.chom.2016.03.007.
32. Zauri M, Berridge G, Thézénas ML, Pugh KM, Goldin R, Kessler BM*, et al.* CDA directs metabolism of epigenetic nucleosides revealing a therapeutic window in cancer. Nature **2015**;524(7563):114-8 doi 10.1038/nature14948.
33. Snyder EL, Watanabe H, Magendantz M, Hoersch S, Chen TA, Wang DG*, et al.* Nkx2-1 represses a latent gastric differentiation program in lung adenocarcinoma. Mol Cell **2013**;50(2):185-99 doi 10.1016/j.molcel.2013.02.018.
34. Yamaguchi T, Hosono Y, Yanagisawa K, Takahashi T. NKX2-1/TTF-1: an enigmatic oncogene that functions as a double-edged sword for cancer cell survival and progression. Cancer Cell **2013**;23(6):718-23 doi 10.1016/j.ccr.2013.04.002.
35. Winslow MM, Dayton TL, Verhaak RG, Kim-Kiselak C, Snyder EL, Feldser DM*, et al.* Suppression of lung adenocarcinoma progression by Nkx2-1. Nature **2011**;473(7345):101-4 doi 10.1038/nature09881.
36. Quezada SA, Peggs KS, Simpson TR, Allison JP. Shifting the equilibrium in cancer immunoediting: from tumor tolerance to eradication. Immunol Rev **2011**;241(1):104-18 doi 10.1111/j.1600-065X.2011.01007.x.
37. Guo X, Zhang Y, Zheng L, Zheng C, Song J, Zhang Q*, et al.* Global characterization of T cells in non-small-cell lung cancer by single-cell sequencing. Nat Med **2018**;24(7):978-85 doi 10.1038/s41591-018-0045-3.
38. Seliger B, Maeurer MJ, Ferrone S. TAP off--tumors on. Immunol Today **1997**;18(6):292-9 doi 10.1016/s0167-5699(97)01052-9.
39. Perry JSA, Russler-Germain EV, Zhou YW, Purtha W, Cooper ML, Choi J*, et al.* Transfer of Cell-Surface Antigens by Scavenger Receptor CD36 Promotes Thymic Regulatory T Cell Receptor Repertoire Development and Allo-tolerance. Immunity **2018**;48(5):923-36.e4 doi 10.1016/j.immuni.2018.04.007.
40. Barkal AA, Brewer RE, Markovic M, Kowarsky M, Barkal SA, Zaro BW*, et al.* CD24 signalling through macrophage Siglec-10 is a target for cancer immunotherapy. Nature **2019**;572(7769):392-6 doi 10.1038/s41586-019-1456-0.

bioRxiv preprint doi: https://doi.org/10.1101/2020.09.04.283739; this version posted September 4, 2020. The copyright holder for this preprint (which was not certified by peer review) is the author/funder. All rights reserved. No reuse allowed without permission.

41. Kristiansen G, Schlüns K, Yongwei Y, Denkert C, Dietel M, Petersen I. CD24 is an independent prognostic marker of survival in nonsmall cell lung cancer patients. British Journal of Cancer **2003**;88(2):231-6 doi 10.1038/sj.bjc.6600702.
42. Slyper M, Porter CBM, Ashenberg O, Waldman J, Drokhlyansky E, Wakiro I*, et al.* A single-cell and single-nucleus RNA-Seq toolbox for fresh and frozen human tumors. Nature Medicine **2020**;26(5):792-802 doi 10.1038/s41591-020-0844-1.
43. Satija R, Farrell JA, Gennert D, Schier AF, Regev A. Spatial reconstruction of single-cell gene expression data. Nat Biotechnol **2015**;33(5):495-502 doi 10.1038/nbt.3192.
44. Korsunsky I, Millard N, Fan J, Slowikowski K, Zhang F, Wei K*, et al.* Fast, sensitive and accurate integration of single-cell data with Harmony. Nature Methods **2019**;16(12):1289-96 doi 10.1038/s41592-019-0619-0.
45. Becht E, McInnes L, Healy J, Dutertre CA, Kwok IWH, Ng LG*, et al.* Dimensionality reduction for visualizing single-cell data using UMAP. Nat Biotechnol **2018** doi 10.1038/nbt.4314.
46. Kiselev VY, Kirschner K, Schaub MT, Andrews T, Yiu A, Chandra T*, et al.* SC3: consensus clustering of single-cell RNA-seq data. Nature Methods **2017**;14(5):483-6 doi 10.1038/nmeth.4236.
47. Sade-Feldman M, Yizhak K, Bjorgaard SL, Ray JP, de Boer CG, Jenkins RW*, et al.* Defining T Cell States Associated with Response to Checkpoint Immunotherapy in Melanoma. Cell **2018**;175(4):998-1013.e20 doi 10.1016/j.cell.2018.10.038.
48. Hänzelmann S, Castelo R, Guinney J. GSVA: gene set variation analysis for microarray and RNA-Seq data. BMC Bioinformatics **2013**;14(1):7 doi 10.1186/1471-2105-14-7.
49. Cao J, Spielmann M, Qiu X, Huang X, Ibrahim DM, Hill AJ*, et al.* The single-cell transcriptional landscape of mammalian organogenesis. Nature **2019**;566(7745):496-502 doi 10.1038/s41586-019-0969-x.
50. Robinson JT, Thorvaldsdóttir H, Wenger AM, Zehir A, Mesirov JP. Variant Review with the Integrative Genomics Viewer. Cancer Res **2017**;77(21):e31-e4 doi 10.1158/0008-5472.Can-17-0337.

bioRxiv preprint doi: https://doi.org/10.1101/2020.09.04.283739; this version posted September 4, 2020. The copyright holder for this preprint (which was not certified by peer review) is the author/funder. All rights reserved. No reuse allowed without permission.

FIGURE LEGENDS

Figure 1. Dissecting early-stage LUAD and the peripheral lung ecosystem using single-cell RNA sequencing. A, Workflow showing multi-region sampling strategy of five LUADs and fourteen spatially defined normal lung tissues for analysis by scRNA-seq. Dis, distant normal; Int, intermediate normal; Adj, adjacent normal; LUAD, tumor tissue. **B**, Uniform manifold approximation and projection (UMAP) embedding of cells from tumor, adjacent normal and distant normal samples of patient one (P1). Cells are colored by their inferred cell types. **C**, Cell composition in absolute cell numbers (stacked bar plots) and relative fractions (pie charts) in each spatial field sample derived from P1. **D**, UMAP view of cells from all five patients, including EPCAM+ and EPCAM- pre-enriched cells from P2-P5. Colors represent assigned major cell types. Cycling, cycling cells. **E**, UMAP view of cell types by spatial fields. Colors represent assigned cell types as in panel D. Lollipop plots indicate, for each major cell type, the relative fraction of cells from each spatial field. Spatial fields are indicated by numbers according to panel A. **F**, Dendrograms showing hierarchical relationships of cells among the spatial fields based on the computed Euclidean distance using transcriptomic features. Dendrograms are shown for five major cell types (from left to right), for all patients together (top) and by patient (bottom). **G**, Same UMAP as in panel D, with further subclustering of lymphoid and myeloid cells. Colors correspond to the cell type annotation in panel H for EPCAM- cells. **H-I**, An area plot showing changes in the relative fractions among the EPCAM- subsets across spatial fields for all patients together and by patient (pie charts, panel I). Stacked bar plots in panel I show absolute cell numbers of the fractions by patient and spatial field**.**

Figure 2. Epithelial lineage diversity and intratumoral heterogeneity in the spatial ecosystem of early-stage LUAD. A, UMAP visualization of all EPCAM+ cells from P1-P5 colored (from left to right) by their assigned cell types, spatial fields, and inferred copy number variation (inferCNV) scores. **B**, Heatmap of major lineage marker genes for EPCAM+ cell clusters (C1-10 as shown in panel A, left), with corresponding bar blots

bioRxiv preprint doi: https://doi.org/10.1101/2020.09.04.283739; this version posted September 4, 2020. The copyright holder for this preprint (which was not certified by peer review) is the author/funder. All rights reserved. No reuse allowed without permission.

outlining relative contribution by spatial field. **C**, Area plot showing changes in EPCAM+ subset fractions across spatial fields. **D**, Representative line plots displaying changes in abundance of non-malignant epithelial cell clusters across spatial fields (identified by the colors of the circles, in the same order as in panel C), with embedded pie charts showing the relative contribution of each spatial field. **E**, Hierarchical relationships of 3 representative subsets of epithelial cells (from top to bottom) among the spatial fields based on the computed Euclidean distance using transcriptomic features (left), and corresponding heatmaps quantifying similarity levels among spatial fields (right). Similarity score is defined as one minus the Euclidean distance. **F**, UMAP plots of cells in the malignant-enriched cluster C9 (panel A), colored by their corresponding patient origin (left), spatial field (middle), and inferCNV score (right). The zoom in view of the right panel shows *KRAS* G12D mutant cells in P2. **G**, Fraction of cells carrying *KRAS* G12D mutation (left bar plot), with numbers indicating the absolute cell numbers, as well as expression levels of *KRAS* (violin plot, top right) and *MUC5AC* (violin plot, bottom right), within cells of each epithelial lineage cluster of P2. **H**, Unsupervised clustering of CNV profiles inferred from scRNA-seq data from patient P3 (left) and P5 (right) tumor samples and demonstrating intratumoral heterogeneity in CNV profiles. Chromosomal amplifications (red) and deletions (blue) are inferred for all 22 chromosomes (color bars on the top). Each row represents a single cell, with corresponding cell type annotated on the right (same as in panel A). **I**, Potential developmental trajectories for EPCAM+ cells from P3 (top) and P5 (bottom) inferred by Monocle 3 analysis. Cells on the tree are colored by pseudotime (dotted boxes) and inferCNV clusters.

Figure 3. Spatial reprogramming of lymphoid subsets towards protumor phenotypes in early-stage LUAD. A, UMAP visualization of lymphoid cell subsets from P1-P5 colored by cell lineage (left) and spatial field (right). CTL, cytotoxic T lymphocyte; Treg, T regulatory cell; ILC, innate lymphoid cell; NK, natural killer cell. **B**, Bubble plot showing the expression of lineage markers. Both the fraction of cells expressing (indicated by the size of the circle) as well as their scaled expression levels (indicated by the color of the circle) are shown. **C**, Changes in the abundance of

bioRxiv preprint doi: https://doi.org/10.1101/2020.09.04.283739; this version posted September 4, 2020. The copyright holder for this preprint (which was not certified by peer review) is the author/funder. All rights reserved. No reuse allowed without permission.

lymphoid cell lineages and cellular states across the LUADs and spatial normal samples. Embedded pie charts show the contribution of each spatial sample to the indicated cell subtype/state. **D**, UMAP plots of CD8+ T lymphocytes colored by cell states (top), spatial field (middle), and cytotoxic score (bottom). The heatmap on the right shows normalized expression of marker genes for defined CD8 T cell subsets. Each column represents a cell. Top annotation tracks indicate (from top to bottom) cell states, naïve T cell scores and cytotoxic scores calculated using curated gene signatures, and the corresponding spatial field of each cell. **E**, Depletion of CD8+ GNLY-hi CTLs in the tumor microenvironment of LUADs. Bar plot (top left) and boxplot (top middle) showing percentage of CD8+ GNLY-hi CTLs among total CD8+ cells from all patients across the spatial fields. Each circle in the boxplot represents a patient sample. *P* - value was calculated using Kruskal-Wallis test. Cytotoxicity signature score (violin plot, top right) of CD8+ CTLs across spatial fields (*, $P < 0.05$; **, $P < 0.01$; ***, $P < 0.001$). *P* - values were calculated using Wilcoxon rank sum test. The percentage of CD8+ CTLs expressing cytotoxic signature genes (indicated by the size of the circle) and their scaled expression levels (indicated by the color of the circle) across the LUADs and spatial normal lung samples (bubble plot, bottom left). Expression levels of *NKG7* and *GNLY* in CD8+ CTLs across the spatial samples (violin plots, bottom right). **F**, UMAP plots of CD4+ T lymphocytes colored by cell states (top), spatial field (middle), and Treg signature score (bottom). The heatmap on the right shows normalized expression of marker genes for CD4+ T cells grouped by defined subcluster. Each column represents a cell. Top annotation tracks indicate (from top to bottom) cell states, Treg signature score, cytotoxic scores, and naïve T cell score calculated using curated gene signatures, and the corresponding spatial field of each cell. **G**, Enrichment of CD4+ T regulatory cells (Treg) in the tumor microenvironment of LUADs. Bar plot (top left) and boxplot (top middle) showing percentage of CD4 Tregs among total CD4+ cells from all patients across the spatial fields. Each circle in the boxplot represents a patient sample. *P* - value was calculated using Kruskal-Wallis test. Percentage of CD4+ Tregs expressing inhibitory immune checkpoint genes (indicated by the size of the circle) and their scaled expression levels (indicated by the color of the circle, color assignment same as panel E) across the spatial samples (bubble plot, top right). Frequency of

bioRxiv preprint doi: https://doi.org/10.1101/2020.09.04.283739; this version posted September 4, 2020. The copyright holder for this preprint (which was not certified by peer review) is the author/funder. All rights reserved. No reuse allowed without permission.

CD4+ Treg cells co-expressing *CTLA4* and *TIGIT* immune checkpoints across the spatial samples (scatter plots, bottom). The fractions of *CTLA4*+*TIGIT*+ Tregs are labeled on each plot.

Figure 4. Reduced signatures of antigen presentation and inflammatory dendritic cells in the microenvironment of early-stage LUAD. A, UMAP visualization of myeloid cell lineages colored by cell type/state (left) and the spatial fields (right). Mac, macrophages; Mono, monocytes; DC, dendritic cell; cDC, classical dendritic cell; pDC, plasmacytoid dendritic cell. **B**, Bubble plot showing the percentage of myeloid cells expressing lineage specific marker genes (indicated by the size of the circle) as well as their scaled expression levels (indicated by the color of the circle). **C**, Changes in the abundance of myeloid cell subsets across the LUADs and spatial normal lung samples. Embedded pie charts show the contribution of each spatial sample to the indicated cell subtype/state. **D**, UMAP plot of monocyte and macrophage subpopulations, color coded by cell type/state (left), spatial field (middle), and antigen presentation score (right). **E**, The percentage of M2-like macrophages cluster 1 expressing antigen presentation genes (indicated by the size of the circle) and their scaled expression levels (indicated by the color of the circle) across the spatial samples (bubble plot). **F**, Ridge plots showing the expression levels of MHC class I and MHC class II genes in M2-like macrophages cluster 1, and across LUADs and spatial normal lung samples. **G**, Violin plots showing the antigen presentation score in M2-like macrophages (clusters 1 and 5) across LUADs and spatial normal lung samples for all patients together (left) and within patients (right) (***, $P < 0.001$). P – values were calculated by Wilcoxon rank sum test. **H**, UMAP plots of dendritic cells, color coded by cell state (left) and spatial field (right). **I**, UMAP plots showing unsupervised subclustering of cDC2 cells colored by cluster ID (top left), spatial field (top right) and the computed inflammatory signature score (bottom). **J**, Heatmap showing normalized expression of marker genes of cDC2 cell subsets. The top annotation tracks indicate (from top to bottom) the inflammatory signature scores, spatial field tissue of origins, and cDC2 cell clusters. **K**, Bubble plot showing the percentage of cDC2 cells expressing inflammatory and non-inflammatory

bioRxiv preprint doi: https://doi.org/10.1101/2020.09.04.283739; this version posted September 4, 2020. The copyright holder for this preprint (which was not certified by peer review) is the author/funder. All rights reserved. No reuse allowed without permission.

signature genes (indicated by the size of the circle) as well as their scaled expression levels (indicated by the color of the circle) in the LUADs and spatial normal lung tissues. **L**, **M**, Depletion of inflammatory cDC2 cluster C2 cells in the tumor microenvironment of LUADs. Bar plot (**L**) and boxplot (**M**) showing fraction of cDC2 C2 cells among total cDC2 cells and across the LUADs and spatial normal lung tissues. Individual circles in (**M)** correspond to patient samples. *P* - value was calculated using Kruskal-Wallis test. **N**, Violin plot showing the inflammatory signature scores in cDC2 C2 cells across LUADs and spatial normal lung samples. **O,** boxplot showing the inflammatory signature score in normal lung (NL), in premalignant atypical adenomatous hyperplasia (AAH) and in LUAD from an independent cohort (*, $P < 0.05$; **, $P < 0.01$; ***, $P < 0.001$; N.S, $P > 0.05$ of the Wilcoxon rank sum test).

Figure 5. Enriched ligand-receptor cell-cell communication networks between LUADs and their immune microenvironment. **A**, Computational analysis workflow of cell-cell communication using iTALK to identify, from a database of curated ligand-receptor (L-R) pairs, the highly expressed immune checkpoint- and cytokine-receptor pairs, that are significantly and differentially altered (i.e. interactions lost or gained) between LUADs and spatial normal lung tissues. **B**, Heatmaps showing the overlap (quantified by Jaccard index) of predicted ligand-receptor based interactions among individual LUADs and their corresponding spatially distributed normal lung tissues. **C**, Representative circos plots showing details of immune checkpoint-mediated L-R pairs compared between each of the LUADs of patients 2, 3, and 5, and selected matching spatial normal lung samples. **D**, Violin plots showing expression of the ligand and receptor genes (selected from panel C) involving immune checkpoints and showing spatial gain-of-interaction patterns as highlighted in panel C. **E,** Boxplot showing *CD24* expression levels in an independent cohort of normal lung tissues (NL), premalignant atypical adenomatous hyperplasias (AAH) and LUADs assessed using the Nanostring immune Counter panel (see Supplementary Methods) (*, $P < 0.05$; **, $P < 0.01$; ***, $P < 0.001$; N.S, $P > 0.05$ of the Wilcoxon rank sum test). **F**, Scatterplots using Pearson correlation coefficients between levels of *CD24* with *EPCAM* and *PRF1* in the NL, AAH,

bioRxiv preprint doi: https://doi.org/10.1101/2020.09.04.283739; this version posted September 4, 2020. The copyright holder for this preprint (which was not certified by peer review) is the author/funder. All rights reserved. No reuse allowed without permission.

and LUAD samples. **G**, Boxplot depicting *CD24* expression levels in LUADs and matched normal lung tissues (NL) from the TCGA LUAD cohort (*, $P < 0.05$; **, $P < 0.01$; ***, $P < 0.001$; N.S, $P > 0.05$ of the Wilcoxon rank sum test). **H**, Scatterplots showing correlation of expression using Pearson's correlation coefficients between *CD24* with *EPCAM* and *PRF1*.

Supplementary Figure Legends

Supplementary Figure S1. Quality control metrics and expression of cell lineage markers across the spatial LUAD scRNA-seq dataset. A, Statistical summary of cells passing quality control (QC) and showing cell number (left), fraction of mitochondrial genes (middle), and the number of detected genes (right) per sample. Dis, distant normal; Int, intermediate normal; Adj, adjacent normal; LUAD, tumor tissue. **B-C,** UMAP plots showing cells colored by patient ID (B) and sample batch (C). **D-E,** Bubble plots showing the percentage of cells expressing lineage markers (indicated by the size of the circle) as well as their scaled expression levels (indicated by the color of the circle) across all cells (D; related to main Fig. 1D and E) or selected cell types (E; related to main Fig. 1 G and H). NK; natural killer cell, DC; dendritic cell, EC; endothelial cell.

Supplementary Figure S2. Trajectory analysis of alveolar cells and copy number inference of malignant-enriched cells. A, UMAP view showing *EPCAM*+ cells colored by sample batch. **B,** Bar plot showing absolute numbers of cells for each lung epithelial cell lineage. Dis, distant normal; Int, intermediate normal; Adj, adjacent normal; LUAD, tumor tissue; AT1, alveolar type 1; AT2, alveolar type 2. **C,** Potential developmental trajectory for alveolar cells inferred by pseudotime analysis. Cells were ordered by pseudotime (dotted box) and colored by alveolar cell state. **D,** Bubble plots showing the percentage (indicated by the size of the circle) of cells expressing markers of alveolar states shown in trajectory analysis from panel C as well as their scaled expression levels (indicated by the color of the circle). **E,** Pseudotime trajectory in C showing cells colored by Notch signaling signature score. **F,** Plots showing Notch signaling signature score among alveolar cell states in trajectory analysis from panel E. **G,** Heatmap showing inferCNV score of cells in the malignant-enriched cluster. **H,** UMAP plots

bioRxiv preprint doi: https://doi.org/10.1101/2020.09.04.283739; this version posted September 4, 2020. The copyright holder for this preprint (which was not certified by peer review) is the author/funder. All rights reserved. No reuse allowed without permission.

showing reclustering of malignant-enriched cells and highlighting those from patient 2 in red (P2; top). Bottom UMAP shows reclustering of P2 malignant-enriched cells and identifies (with red asterisk) those harboring *KRAS*-G12D mutation. **I,** Heatmap showing highly expressed genes among sub-clusters (subcluster of cells enriched with *KRAS* G12D mutations compared to subclusters lacking the mutation) identified in the bottom UMAP of panel H.

Supplementary Figure S3. Reprogramming of lymphoid cell subsets towards an immune suppressive tumor microenvironment in early-stage LUAD. A, UMAP of lymphoid cells colored by sample batch. **B,** Bar plots showing the absolute numbers of each lymphoid cell subset in each spatial sample. Dis, distant normal; Int, intermediate normal; Adj, adjacent normal; LUAD, tumor tissue; CTL, cytotoxic T lymphocyte; Treg, T regulatory cell; ILC, innate lymphoid cell; NK, natural killer cell. **C,** Changes in the abundance of specific lymphoid cellular lineages and states across the LUADs and spatial normal samples. Embedded pie charts show the contribution of each spatial sample to the indicated cell subtype/state. **D,** Cytotoxicity signature score in CD8+ *GNLY*_hi CTLs in patient three (P3, left) and in patient 4 (P4, right) across spatial fields (*, $P < 0.05$; **, $P < 0.01$; ***, $P < 0.001$ of the Wilcoxon rank sum test). **E,** Treg signature score in T regulatory cells across spatial fields in all patients (left), P3 (middle) and in patient 5 (P5, right) (*, $P < 0.05$; **, $P < 0.01$; ***, $P < 0.001$ of the Wilcoxon rank sum test). **F,** Depletion of CD4+ CTLs in the tumor microenvironment of LUAD. Boxplot showing percentage of CD4+ CTLs *GZMA*-hi among total CD4+ cells from all patients across the spatial fields. Each circle represents a patient sample. *P* - value was calculated using Kruskal-Wallis test. **G,** Violin plots showing cytotoxic signature score in CD4+ CTL *GZMA*-hi cells from all patients (left) and P5 (right; *, $P < 0.05$; **, $P < 0.01$; ***, $P < 0.001$ of the Wilcoxon rank sum test). **H,** Frequency of CD4+ CTL *GZMA***-**hi cells co-expressing *GZMA* and *GZMH* across the spatial samples. The fractions of *GZMA*+*GZMH*+ *CD4*+ CTLs are labeled on each plot. **I-K,** Expression profiling of different isotypes of plasma cells across the spatial samples. **I,** Heatmap showing isotype genes expression in plasma cells. **J,** Bar plots showing plasma cell isotype composition across spatial fields. **K,** Dot plots showing the fractional change of IGHA1/2

bioRxiv preprint doi: https://doi.org/10.1101/2020.09.04.283739; this version posted September 4, 2020. The copyright holder for this preprint (which was not certified by peer review) is the author/funder. All rights reserved. No reuse allowed without permission.

and IGHG3 across all patients and in each patient (left to right). **L-N,** Reprogramming of B cells in early-stage LUAD. **L,** Heatmap showing unsupervised clustering of B cells sub-populations. **M,** UMAP showing re-clustering of B cells into sub-populations. **N,** Ridge plots (left) showing *RAC2* and *ACTG* expression levels among B cell sub-clusters, and scatter plots (right) showing the frequency of B cells co-expressing *RAC2*+ and *ACTG*+ across spatial fields. The fractions of *RAC2*+*ACTG*+ B cells are labeled on each plot. **O,** Boxplot showing the B cell C0 signature score in normal lung tissues (NL), premalignant atypical adenomatous hyperplasias (AAH) and LUADs in an independent validation cohort. (*, $P < 0.05$; **, $P < 0.01$; ***, $P < 0.001$; N.S, $P > 0.05$). *P* - values were calculated using Wilcoxon rank sum test.

Supplementary Figure S4. Reprogramming of myeloid cells in the tumor microenvironment of early-stage LUAD. A, UMAP view showing myeloid cells colored by sample batch. **B**, Stacked bar plots showing absolute numbers of each lymphoid cell subset across the spatial samples. Dis, distant normal; Int, intermediate normal; Adj, adjacent normal; LUAD, tumor tissue; mono; monocytes, mac; macrophages, cDC; classical dendritic cells, pDC; plasmacytoid dendritic cell. **C,** Changes in the abundance of specific lymphoid cellular lineages and states across the LUADs and spatial normal samples. Embedded pie charts show the contribution of each spatial sample to the indicated cell subtype/state. **D**, Heatmap showing the expression of inflammatory/non-inflammatory signature genes in cDC2 cells. **E**, Boxplot showing the non-inflammatory *versus* inflammatory signature score in normal control (NL), in normal lung tissues (NL), premalignant atypical adenomatous hyperplasias (AAH) and LUADs in an independent validation cohort. (*, $P < 0.05$; **, $P < 0.01$; ***, $P < 0.001$; N.S, $P > 0.05$). *P* - values were calculated using Wilcoxon rank sum test. **F**, Heatmap showing DEGs between LUAD and normal samples in pDCs. **G**, Ridge plots showing the expression level changes of *FOS*, *JUN* and *FOSB* in pDCs and across spatial samples.

Supplementary Figure S5. Composition and gene expression changes in stromal and endothelial sub-populations in early-stage LUAD as well as adjacent and

bioRxiv preprint doi: https://doi.org/10.1101/2020.09.04.283739; this version posted September 4, 2020. The copyright holder for this preprint (which was not certified by peer review) is the author/funder. All rights reserved. No reuse allowed without permission.

more distant normal lung tissues. A, UMAP view of stromal and endothelial cells colored by sample batch. **B**, UMAP view of stromal and endothelial sub-populations. **C**, Bubble plot showing the percentage of stromal and endothelial cells expressing lineage markers (indicated by the size of the circle) as well as their scaled expression levels (indicated by the color of the circle). **D,** Bar plot showing the absolute number of cells from each stromal and endothelial subset. Dis, distant normal; Int, intermediate normal; Adj, adjacent normal; LUAD, tumor tissue; EC, endothelial cells. **E**, Changes in the abundance of stromal and endothelial cell lineages across the LUADs and spatial normal samples. Embedded pie charts show the contribution of each spatial sample to the indicated stromal and endothelial subtype. **F**, Heatmap showing DEGs between LUAD and normal samples in EC venule sub-populations. **G**, Bar plot showing significantly enriched pathways of up/down regulated DEGs in panel F. **H,** Ridge plots showing the expression level changes of *HLA-DPB1*, *IL33*, and *IGFBP7* in EC venule sub-populations and across spatial samples.

Supplementary Figure S6. Enriched ligand-receptor cell-cell communication networks between LUAD and the immune microenvironment. A-B, Circos plot showing additional details of the immune checkpoint-mediated L-R pairs compared between each of the LUADs of patients 5 and select matching spatial normal lung samples. And **B**) Violin plot showing expression of epithelial *LGALS9* (ligand) and dendritic cells *HAVCR2* (receptor) and showing spatial gain-of-interaction patterns as highlighted in the circos plot of patient 5 (P5) in panel A. **C,** Circos plot showing details of chemokine-mediated L-R pairs comparison between the LUAD and tumor-intermediate normal tissue of patient 3 (P3). **D,** Violin plots showing spatial expression of the chemokine and receptor genes in P3 and highlighted in panel C. **E,** Circos plots showing details of chemokine-mediated L-R pairs comparison between the LUAD and tumor-intermediate normal tissue of patient 2 (P2, panel E left) and patient 5 (P5, panel E right). **F**, Violin plots showing spatial expression of the chemokine and receptor genes in P5 and highlighted in panel E right. **G-H,** Scatterplots showing the correlation of expression between *CD24* and other immune-regulated genes in GSE10251 (G) and in

bioRxiv preprint doi: https://doi.org/10.1101/2020.09.04.283739; this version posted September 4, 2020. The copyright holder for this preprint (which was not certified by peer review) is the author/funder. All rights reserved. No reuse allowed without permission.

TCGA (H) LUAD cohorts. Pearson correlation test was used for p-values show in panel G and panel H.

Figure 1

bioRxiv preprint doi: https://doi.org/10.1101/2020.09.04.283739; this version posted September 4, 2020. The copyright holder for this preprint (which was not certified by peer review) is the author/funder. All rights reserved. No reuse allowed without permission.

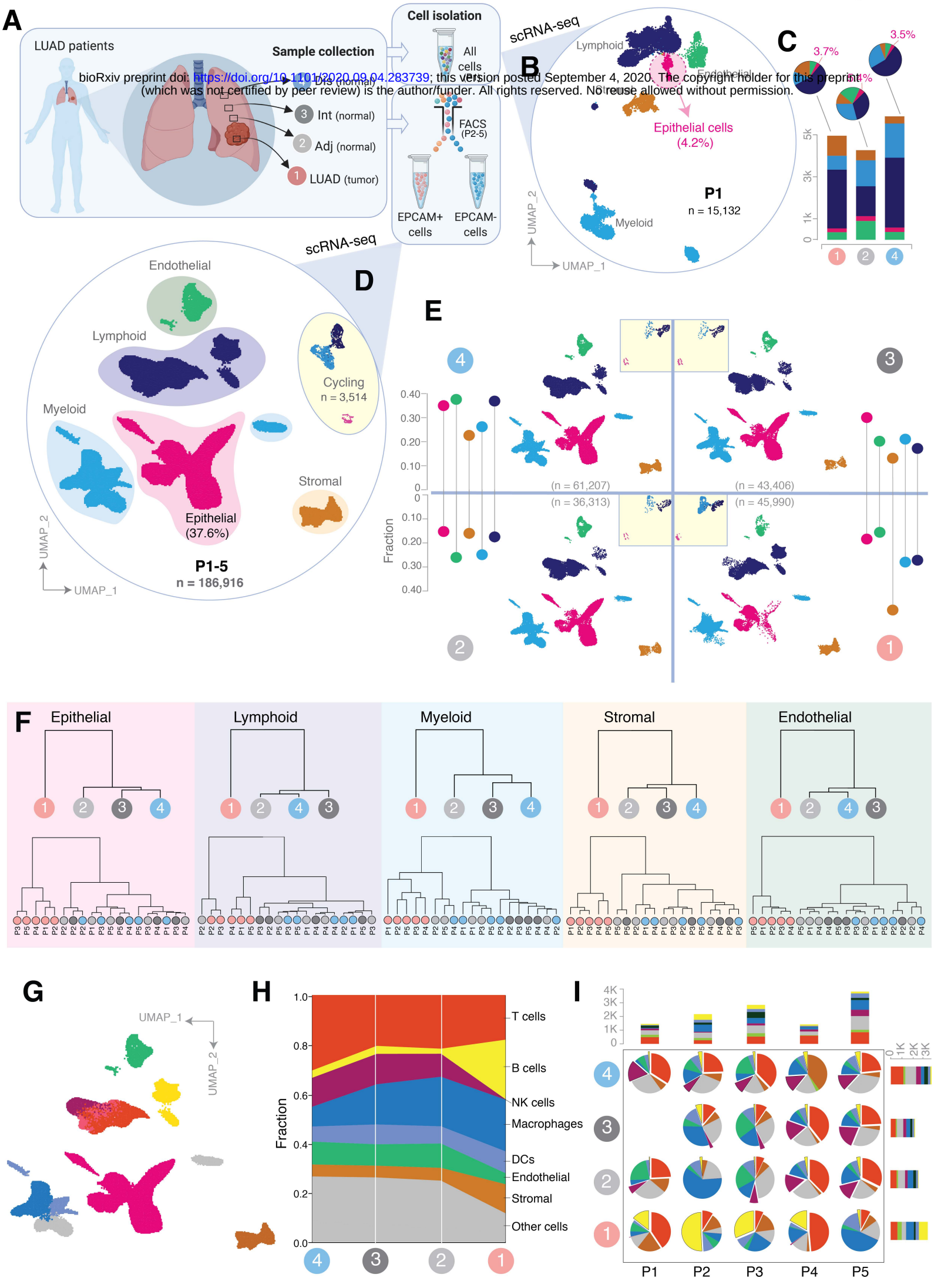

bioRxiv preprint doi: https://doi.org/10.1101/2020.09.04.283739; this version posted September 4, 2020. The copyright holder for this preprint (which was not certified by peer review) is the author/funder. All rights reserved. No reuse allowed without permission.

Figure 2

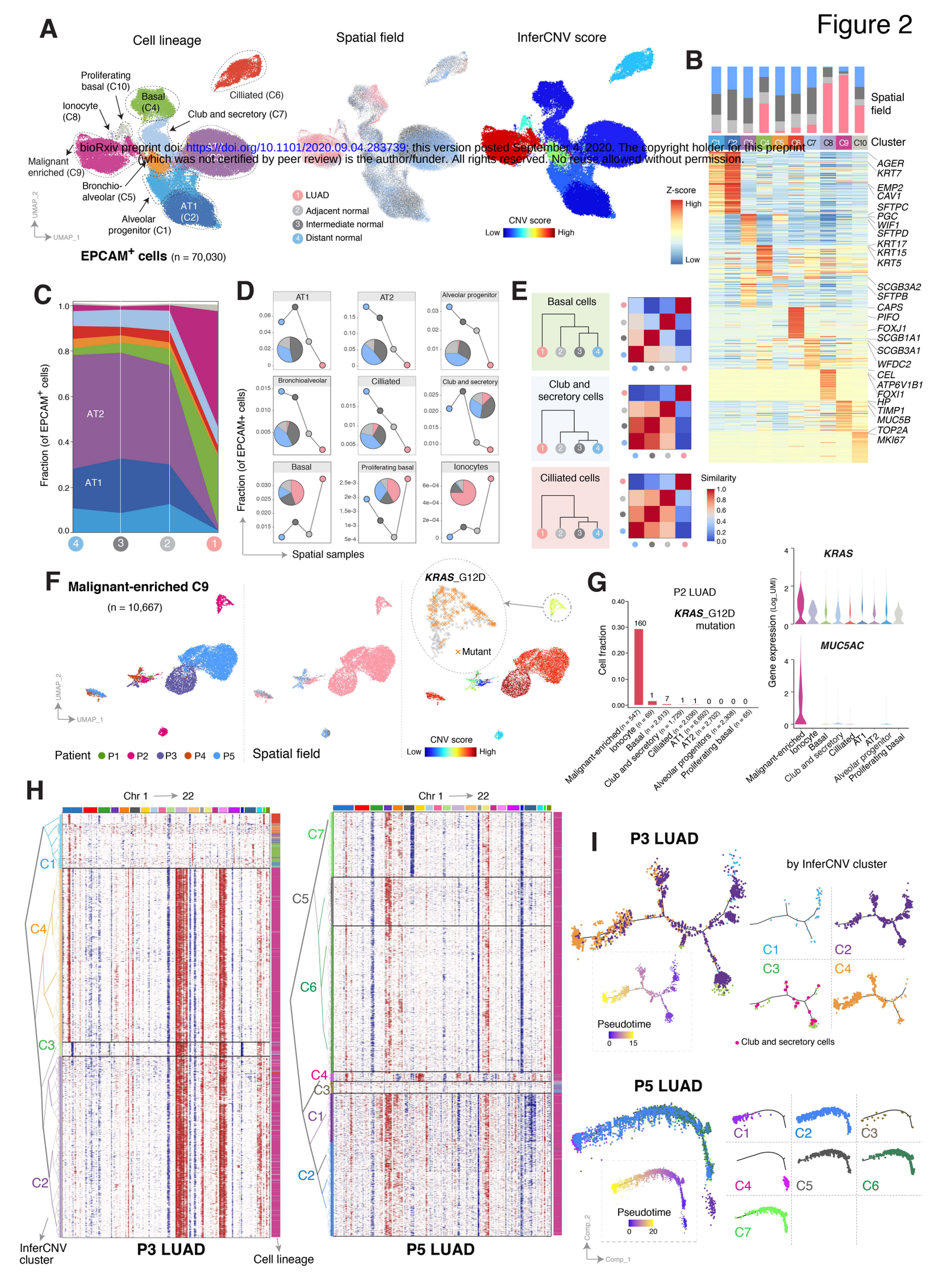

bioRxiv preprint doi: https://doi.org/10.1101/2020.09.04.283739; this version posted September 4, 2020. The copyright holder for this preprint (which was not certified by peer review) is the author/funder. All rights reserved. No reuse allowed without permission.

Figure 3

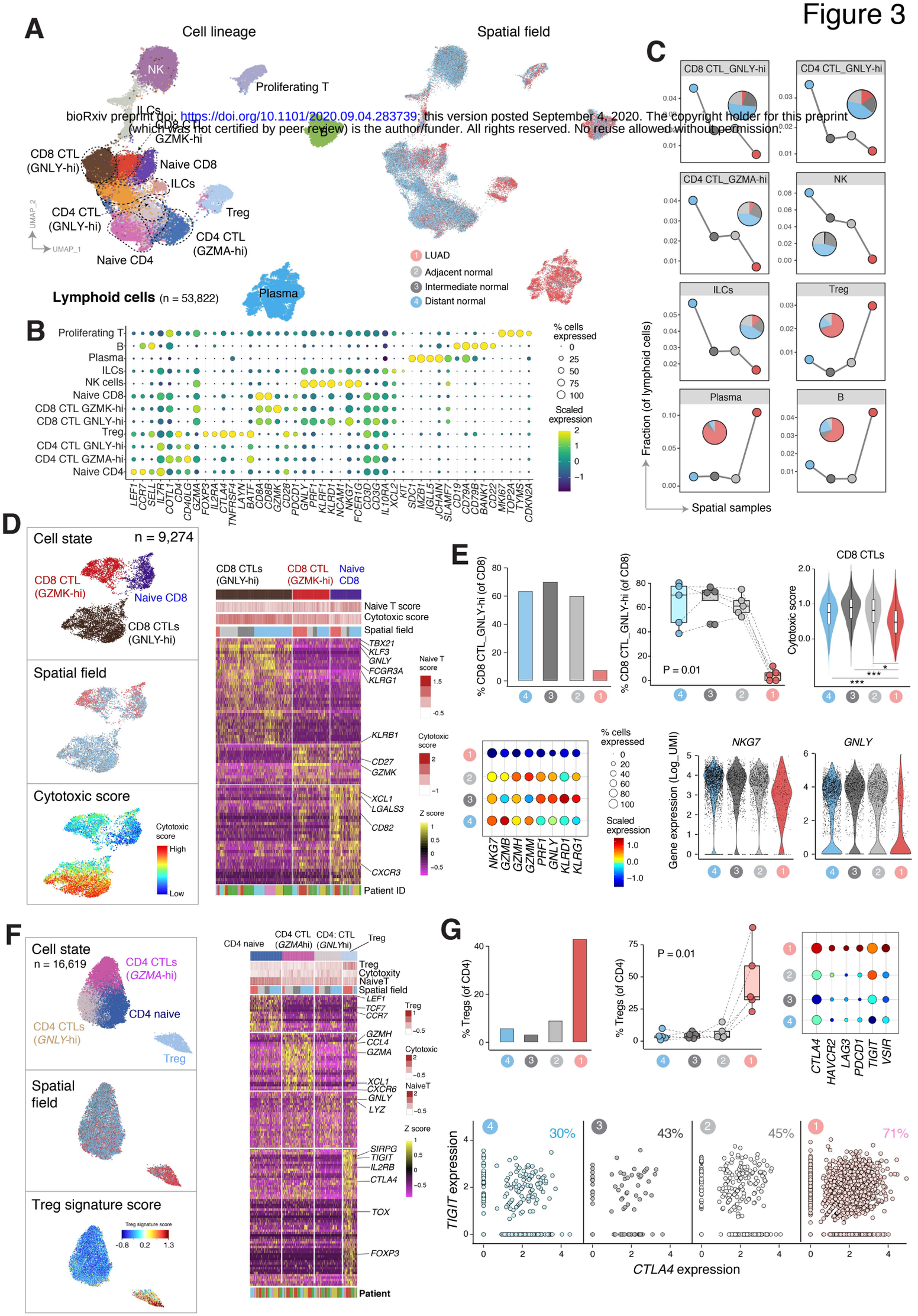

bioRxiv preprint doi: https://doi.org/10.1101/2020.09.04.283739; this version posted September 4, 2020. The copyright holder for this preprint (which was not certified by peer review) is the author/funder. All rights reserved. No reuse allowed without permission.

Figure 4

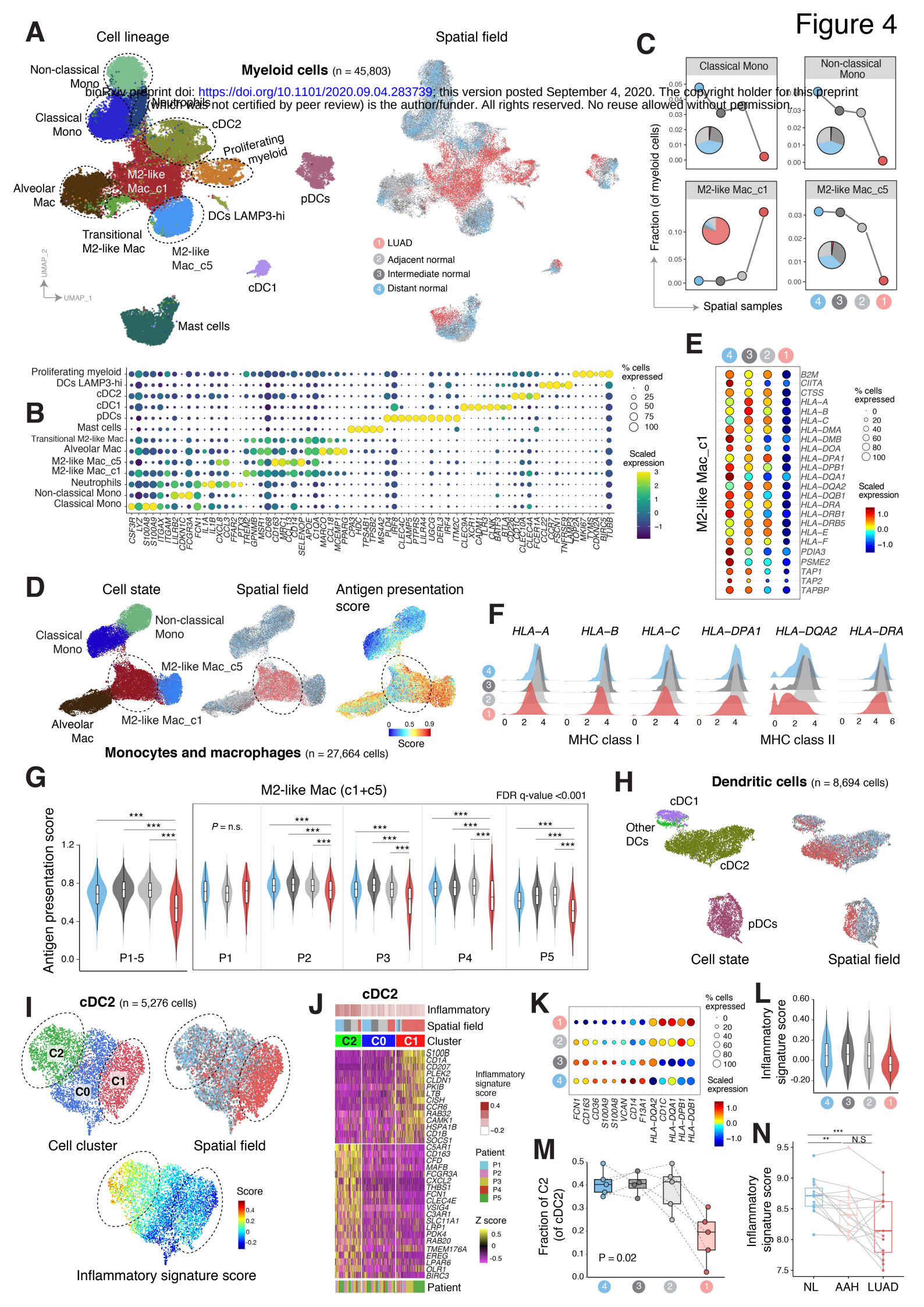

Figure 5

bioRxiv preprint doi: https://doi.org/10.1101/2020.09.04.283739; this version posted September 4, 2020. The copyright holder for this preprint (which was not certified by peer review) is the author/funder. All rights reserved. No reuse allowed without permission.

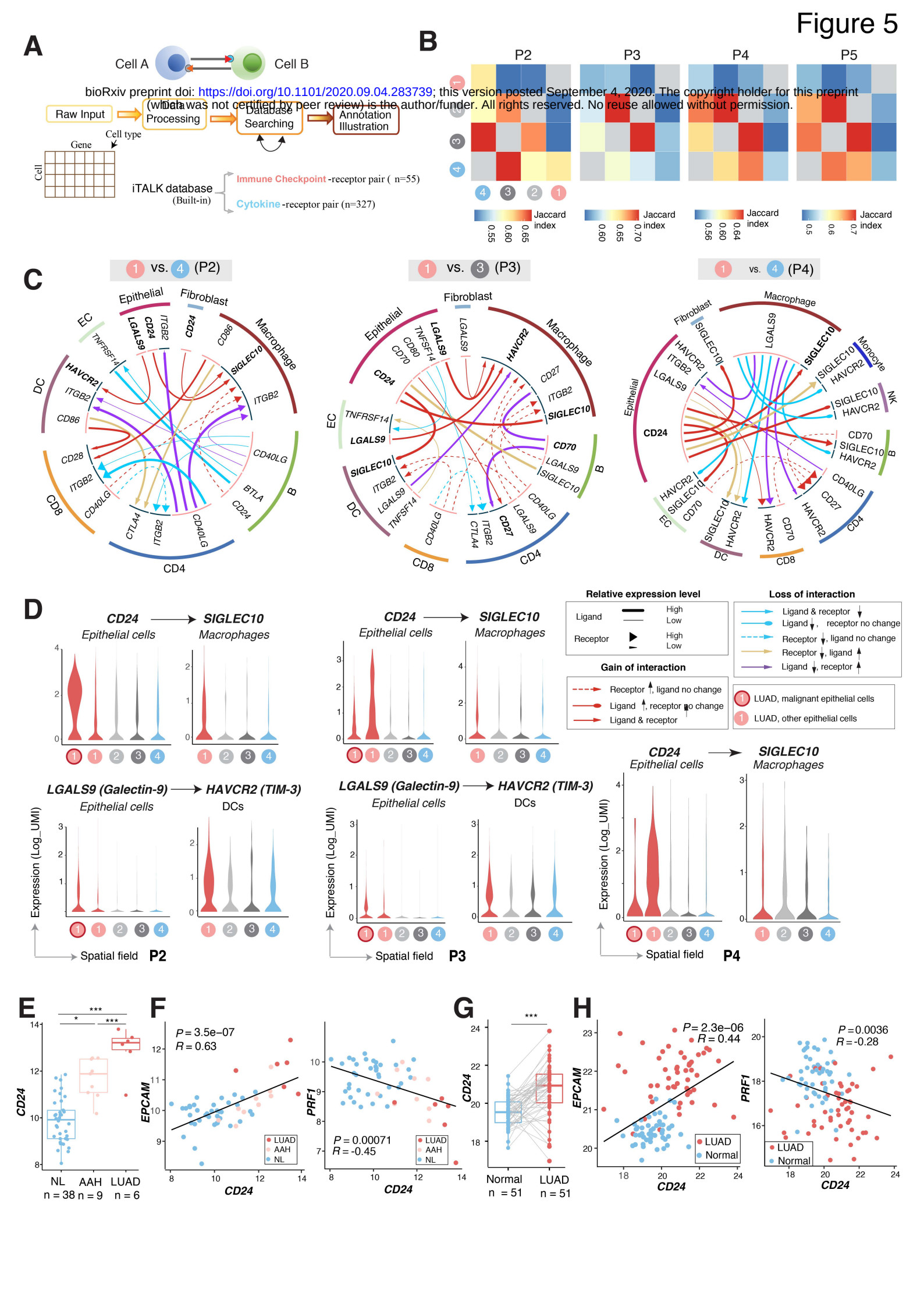

Supplementary figure S1

bioRxiv preprint doi: https://doi.org/10.1101/2020.09.04.283739; this version posted September 4, 2020. The copyright holder for this preprint (which was not certified by peer review) is the author/funder. All rights reserved. No reuse allowed without permission.

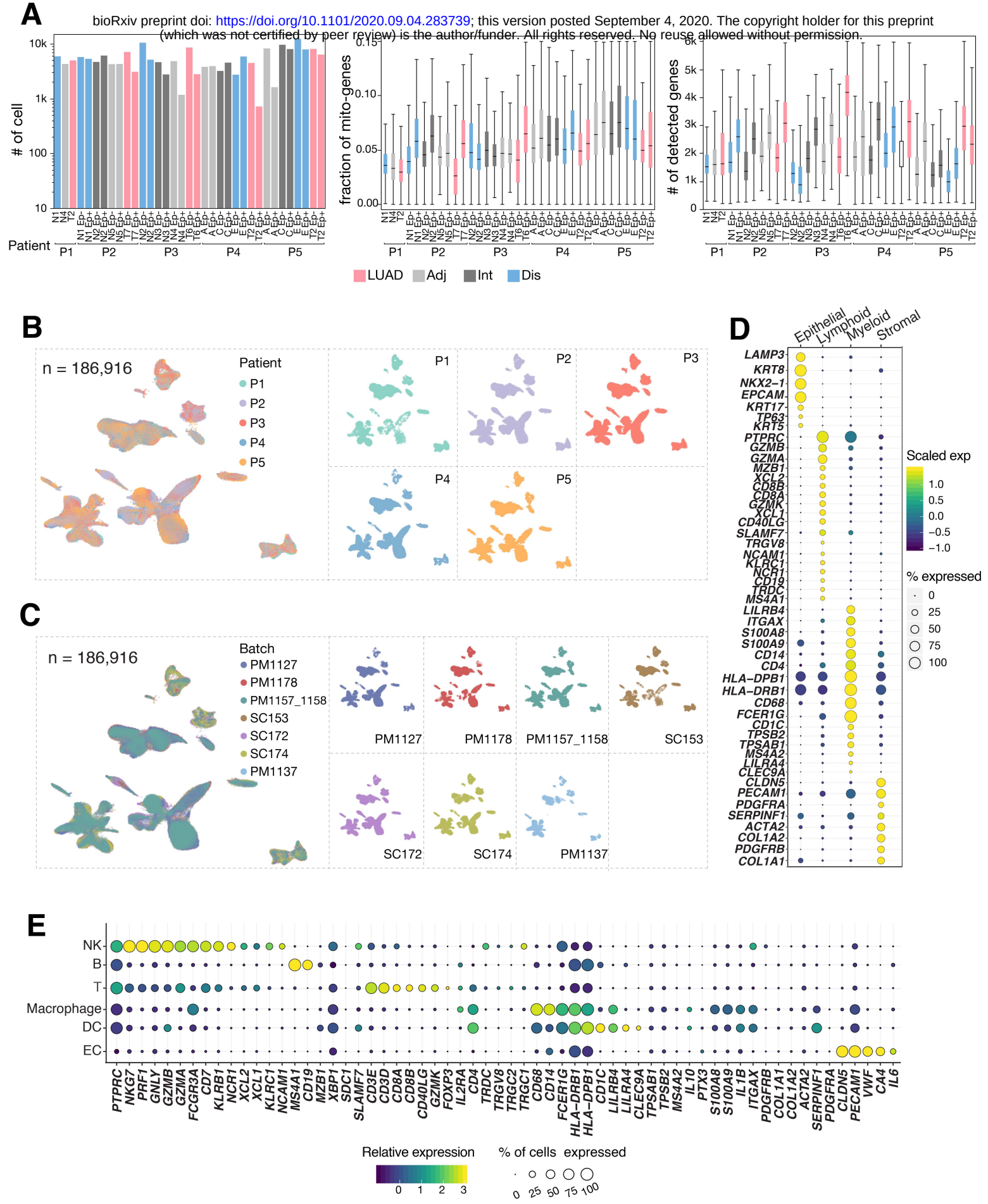

Supplementary figure S2

PMC127 bioRxiv preprint doi: https://doi.org/10.1101/2020.09.04.283739; this version posted September 4, 2020. The copyright holder for this preprint (which was not certified by peer review) is the author/funder. All rights reserved. No reuse allowed without permission.

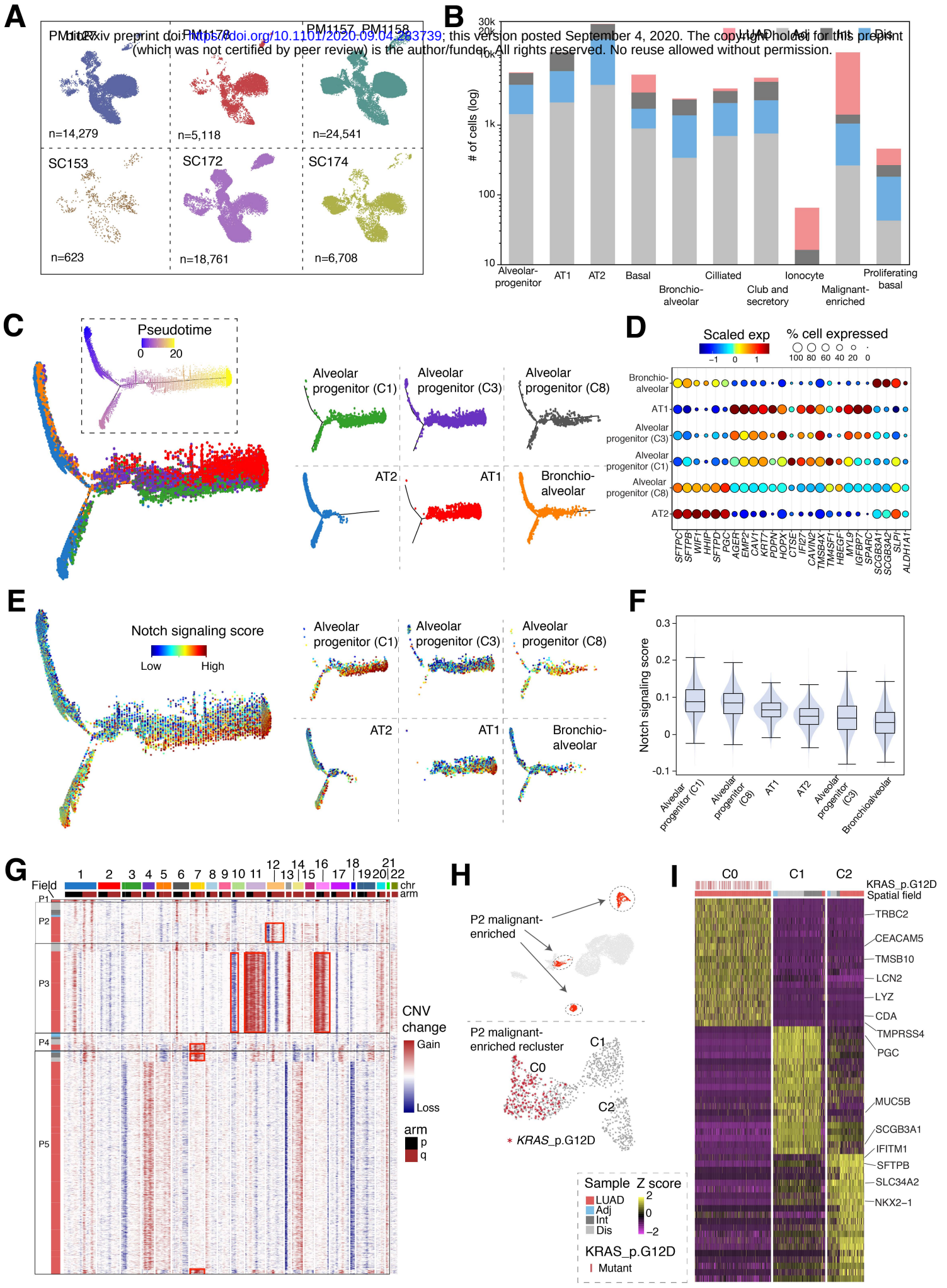

Supplementary figure S3

bioRxiv preprint doi: https://doi.org/10.1101/2020.09.04.283739; this version posted September 4, 2020. The copyright holder for this preprint (which was not certified by peer review) is the author/funder. All rights reserved. No reuse allowed without permission.

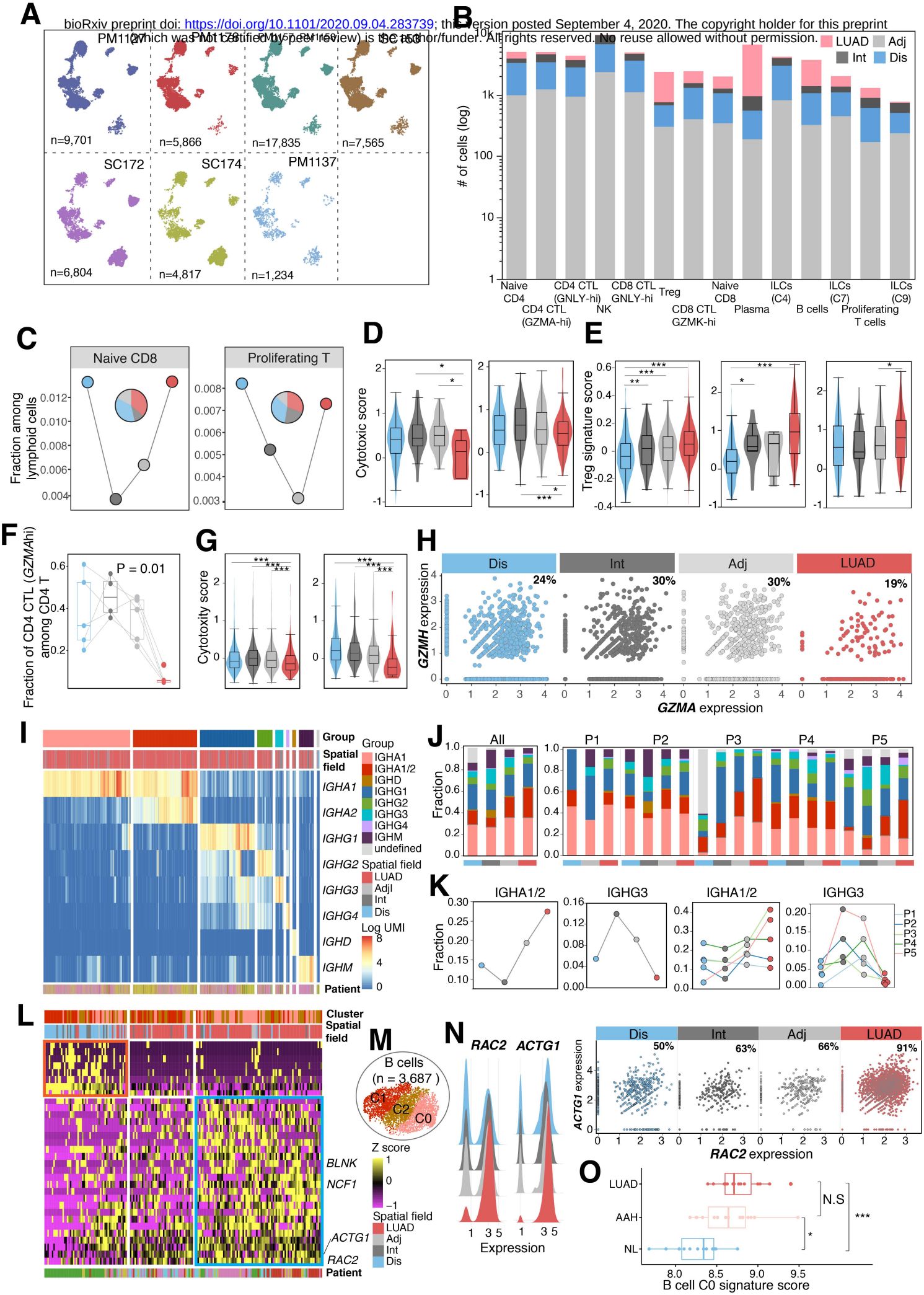

Supplementary figure S4

bioRxiv preprint doi: https://doi.org/10.1101/2020.09.04.283739; this version posted September 4, 2020. The copyright holder for this preprint (which was not certified by peer review) is the author/funder. All rights reserved. No reuse allowed without permission.

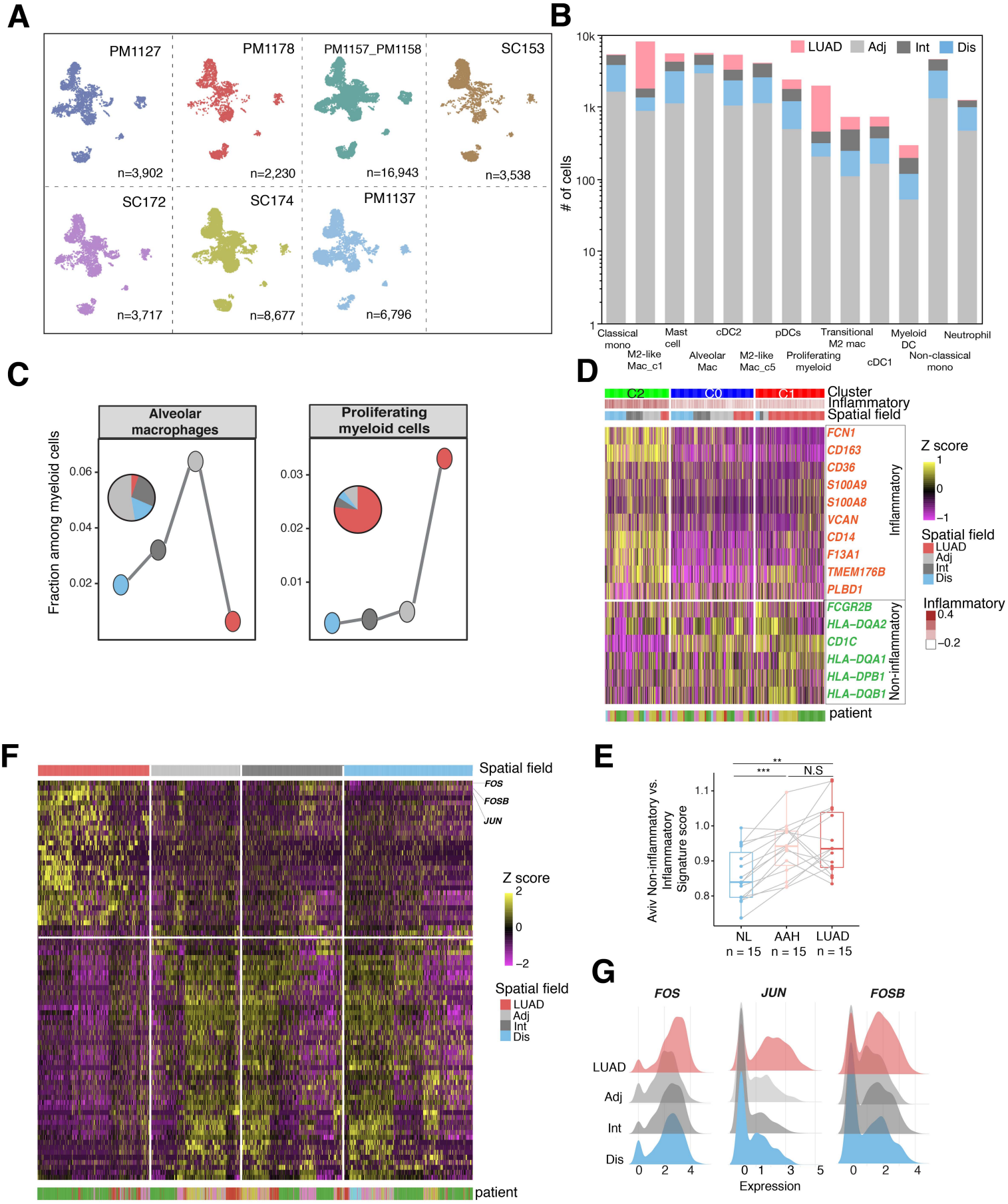

Supplementary figure S5

bioRxiv preprint doi: https://doi.org/10.1101/2020.09.04.283739; this version posted September 7, 2020. The copyright holder for this preprint (which was not certified by peer review) is the author/funder. All rights reserved. No reuse allowed without permission.

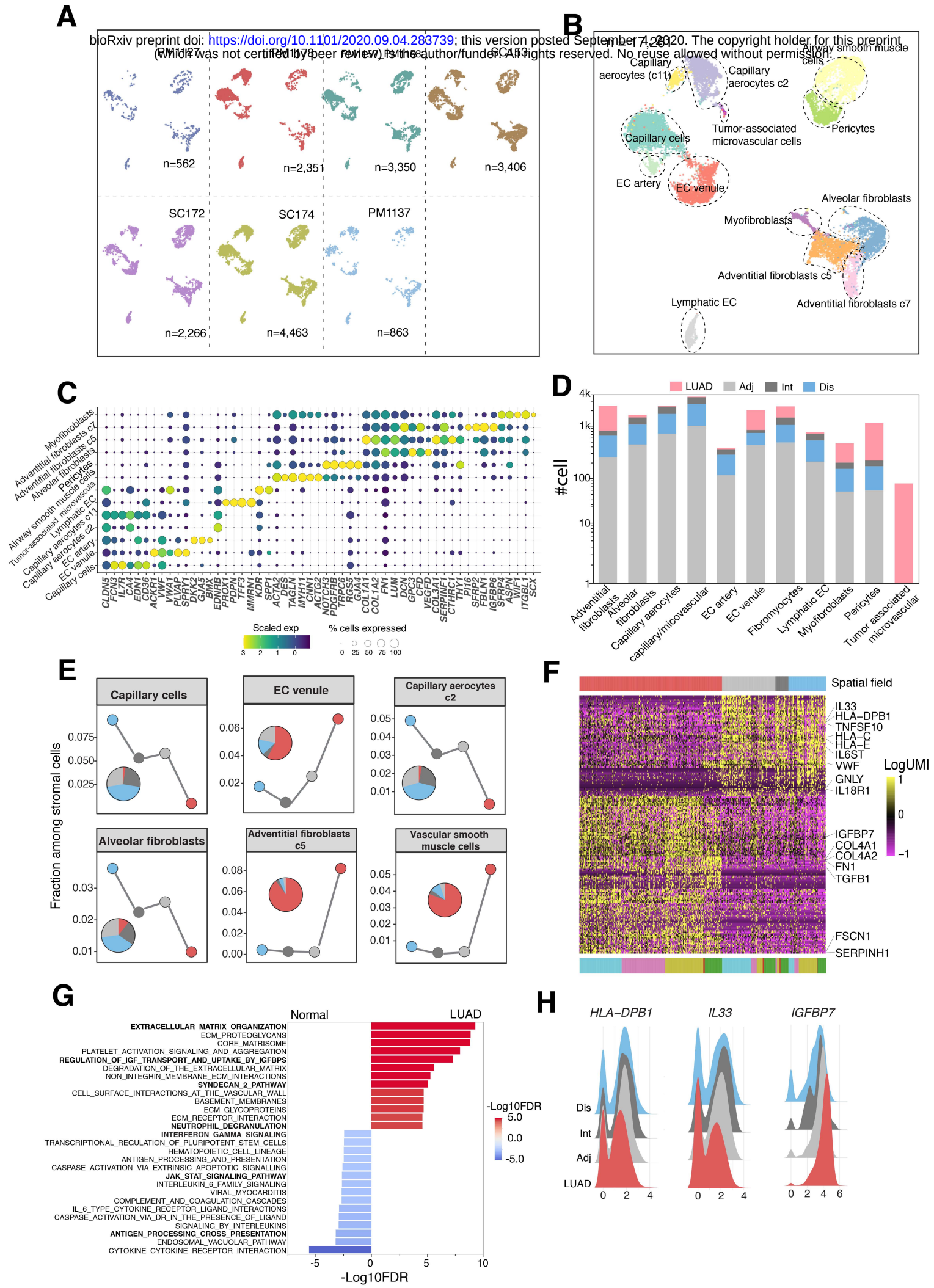

Supplementary figure S6
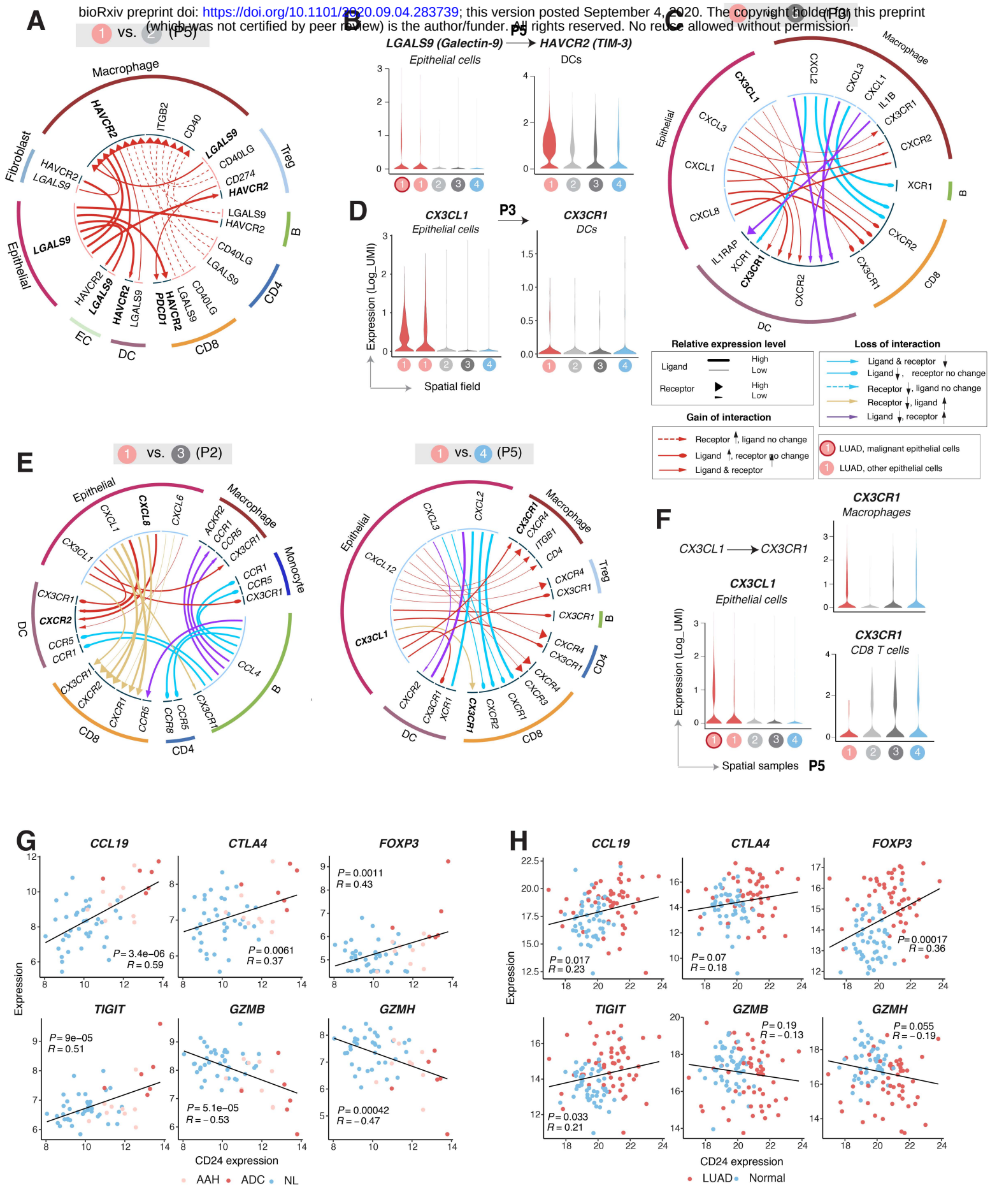
bioRxiv preprint doi: https://doi.org/10.1101/2020.09.04.283739; this version posted September 4, 2020. The copyright holder for this preprint (which was not certified by peer review) is the author/funder. All rights reserved. No reuse allowed without permission.